APPLIED SCIENCES AND ENGINEERING

# Enzyme-like nanoparticle–engineered mesenchymal stem cell secreting HGF promotes visualized therapy for idiopathic pulmonary fibrosis in vivo

**Hongying Bao[1,2], Manxiang Wu[1], Jie Xing[1,2], Zihou Li[1,2], Yuenan Zhang[1,2], Aiguo Wu[1,2]*, Juan Li[1,2]***

Copyright © 2024 The Authors, some rights reserved; exclusive licensee American Association for the Advancement of Science. No claim to original U.S. Government Works. Distributed under a Creative Commons Attribution NonCommercial License 4.0 (CC BY-NC).

**Stem cell therapy is being explored as a potential treatment for idiopathic pulmonary fibrosis (IPF), but its effectiveness is hindered by factors like reactive oxygen species (ROS) and inflammation in fibrotic lungs. Moreover, the distribution, migration, and survival of transplanted stem cells are still unclear, impeding the clinical advancement of stem cell therapy. To tackle these challenges, we fabricate AuPtCoPS trimetallic-based nanocarriers (TBNCs), with enzyme-like activity and plasmid loading capabilities, aiming to efficiently eradicate ROS, facilitate delivery of therapeutic genes, and ultimately improve the therapeutic efficacy. TBNCs also function as a computed tomography contrast agent for tracking mesenchymal stem cells (MSCs) during therapy. Accordingly, we enhanced the antioxidant stress and anti-inflammatory capabilities of engineered MSCs and successfully visualized their biological behavior in IPF mice in vivo. Overall, this study provides an efficient and forward-looking treatment approach for IPF and establishes a framework for a stem cell–based therapeutic system aimed at addressing lung disease.**

## INTRODUCTION

Idiopathic pulmonary fibrosis (IPF) is a highly prevalent and severe form of interstitial lung disease, constituting approximately 40% of all cases within this disease category and seriously affecting human well-being (*1*). It is characterized by the alveolar epithelial cells (AECs) injury, which is accompanied by the heightened activation/stimulation of fibroblasts and myofibroblasts, leading to the buildup of extracellular matrix (ECM) in the alveolar walls (*2*, *3*). Nintedanib and pirfenidone, both Food and Drug Administration–approved therapeutic agents, can slow down the progression of this disease, but they do not significantly extend the survival time of patients in the clinic (*4*, *5*). This deficiency might stem from the drug's ineffectiveness in repairing AEC injury and reducing ECM accumulation, thereby impeding the process of lung tissue remodeling and the enhancement of pulmonary function (*6*, *7*). Recently, mesenchymal stem cells (MSCs) have emerged as a potential cell-based lung regeneration therapy primarily due to their well-established safety profile and remarkable paracrine effects. The effects are characterized by the secretion of a broad spectrum of anti-apoptotic and angiogenic growth factors, which positions MSCs as promising candidates for clinical applications in the field of lung regeneration therapy (*8*, *9*). However, unlike promising outcomes observed in preclinical models, recent meta-analyses have cast doubt on the therapeutic potential of MSC treatment for IPF. While the clinical trials have effectively showcased the feasibility and safety of MSC treatment, the outcomes of these treatments have been deemed unsatisfactory, with no notable improvement in median survival time or lung function of patients (*10*–*12*). These results have led to a consensus regarding the necessity of implementing innovative approaches to enhance the therapeutic efficacy of MSC treatment in IPF.

As a result, various strategies have been used to enhance the therapeutic efficacy of MSCs in IPF therapy. For example, genetically engineered MSCs that overexpress a variety of anti-apoptotic proteins, growth factors, or pro-survival genes have been shown to enhance the survival and retention of MSCs in vivo, ultimately leading to improved pulmonary function in IPF (*13*–*16*). Hepatocyte growth factor (HGF) is a prominent paracrine factor that is secreted by MSCs, exhibiting notable properties of anti-inflammatory, anti-apoptotic, and pro-angiogenic nature, which can contribute to the facilitation of AEC repair and the reduction of ECM deposition (*16*–*18*). Our previous studies have also substantiated that HGF plays a pivotal factor in the therapeutic intervention of IPF by MSCs and observed that MSCs with overexpressed HGF exhibit a more pronounced therapeutic effect on IPF (*19*, *20*). However, IPF tissues exhibit an increased generation of reactive oxygen species (ROS), leading to impaired mitochondrial function and DNA damage in transplanted MSCs, ultimately culminating in the demise of MSCs (*21*, *22*). Therefore, there is an urgent need to develop nanocarriers with enzyme-like activity to enhance the resistance of HGF-overexpressing MSCs to ROS-induced oxidative stress. Given the intricate nature of the fibrotic pulmonary microenvironment, which involves the coexistence of multiple ROS, it is imperative for nanozymes to exhibit not only robust catalytic activity but also remarkable catalytic diversity. Multimetallic nanozymes demonstrate excellent catalytic activity and selectivity owing to their efficient charge-transfer capability and the potential synergistic effect arising from the coexistence of multiple elements (*23*). Hence, the development of multimetallic-based nanocarriers capable of delivering HGF genes and scavenging ROS will greatly improve the antifibrotic and antioxidative stress capabilities of transplanted MSCs.

In addition, the real-time visualization of the MSCs' efficacy in vivo is of great significance in optimizing the MSC-based treatment strategy for IPF. Advanced imaging modalities, including computed tomography (CT), bioluminescence imaging (BLI), magnetic

[1]Ningbo Key Laboratory of Biomedical Imaging Probe Materials and Technology, CAS Key Laboratory of Magnetic Materials and Devices, Laboratory of Advanced Theranostic Materials and Technology, Ningbo Institute of Materials Technology and Engineering, Chinese Academy of Sciences, Ningbo 315201, China. [2]Zhejiang International Cooperation Base of Biomedical Materials Technology and Application, Zhejiang Engineering Research Center for Biomedical Materials, Ningbo Cixi Institute of Biomedical Engineering, Cixi 315300, China.
*Corresponding author. Email: aiguo@nimte.ac.cn (A.W.); lij@nimte.ac.cn (J.L.)

resonance imaging, positron emission tomography, and fluorescence imaging, are presently used for monitoring the localization and dynamics of MSCs after in vivo transplantation (*24*–*26*). In our prior study, on the basis of the application of therapeutic visualization, we specifically designed and developed a series of nanoprobes for visualizing various disease therapies (*27*, *28*). Because of the distinctive properties of lung tissue, such as its low hydrogen proton density, CT imaging technology is widely regarded as a more appropriate approach for visualizing lung diseases in the clinic. Nevertheless, the incorporation of in vivo CT tracers for transplanted MSCs, the delivery of the HGF gene, and mitigating ROS to enhance the efficacy of MSCs in the treatment of IPF pose an unresolved challenge.

Here, we successfully fabricated AuPtCoPS trimetallic-based nanocarriers (TBNCs), through a facile method involving protamine sulfate (PS) as the raw material, and the prepared TBNCs exhibit exceptional characteristics in terms of plasmid DNA (pDNA) loading capacity, enzyme-like activity, and CT imaging performance. Positively charged PS can effectively interact with negatively charged pDNA through electrostatic interaction and facilitate the efficient transportation of pDNA into the nucleus due to PS's remarkable ability for membrane translocation and nuclear localization (*29*). The noble metal gold (Au), renowned for its exceptional conductivity, can enhance electron transfer during catalytic processes, while the platinum (Pt) and cobalt (Co) have inherent superoxide dismutase (SOD)–like and catalase (CAT)-like properties, enabling them to effectively scavenge hydroxyl radicals (•HO) and hydrogen peroxide ($H_2O_2$) (*30*–*32*). In addition, Au and Pt, being high-order metals, exhibit robust x-ray attenuation coefficients, rendering them highly suitable as contrast agents for CT imaging. On the basis of these remarkable properties, the engineered MSCs exhibit notable functions, such as the effective clearance of ROS from fibrotic lungs and efficient expression of HGF at the lesion site, thereby improving the antioxidative stress and antifibrosis capabilities of transplanted MSCs, ultimately prolonging in vivo survival time to an unprecedented 14 days of transplanted MSCs and significantly improving the therapeutic effect on IPF. In addition, engineered MSCs are endowed with CT imaging capability, which allows for the real-time monitoring of the in vivo biological behavior of transplanted MSCs and facilitates the visualization of the efficacy of transplanted MSCs on IPF (Fig. 1). Collectively, we anticipate that this study will provide a

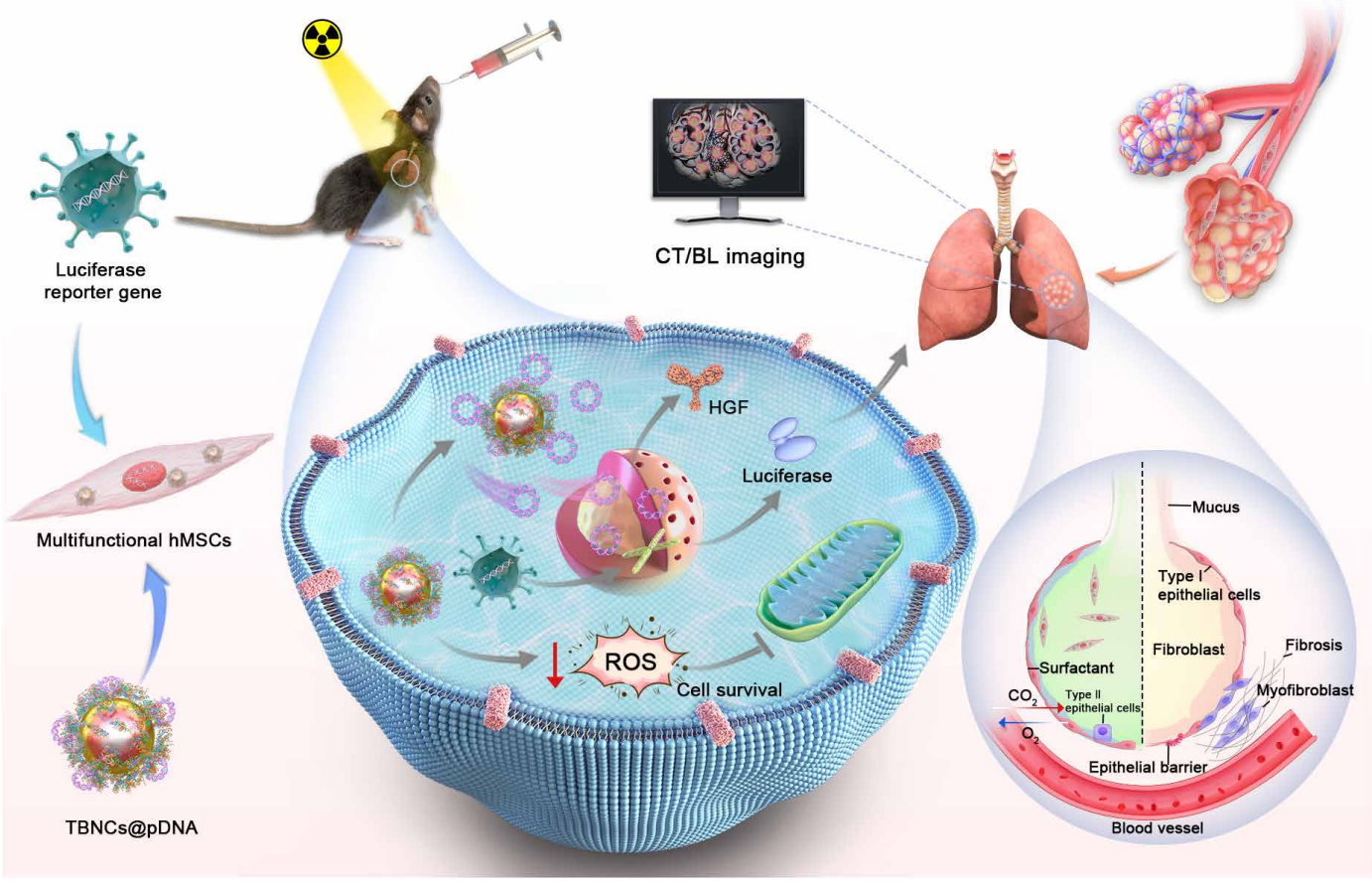


**Fig. 1. Schematic illustration of the application of TBNCs@pDNA in gene delivery and dual-modal imaging to track hMSCs in the treatment of IPF.** TBNCs loaded with HGF pDNA (TBNCs@pDNA) were cocultured with human MSCs (hMSCs) that constitutively expressed the luciferase reporter gene to generate multifunctional hMSCs. Subsequently, these multifunctional hMSCs were administered into the lungs of IPF mice via the trachea to facilitate the regeneration of damaged AECs and the reduction of collagen accumulation in the lung interstitium, thereby enhancing the gas exchange function of the alveoli. In addition, CT/BL imaging modalities were used to monitor the in vivo distribution, migration, and viability of the transplanted hMSCs in real time.

promising perspective on the utilization of engineered MSC-based therapy for the treatment of IPF.

## RESULTS AND DISCUSSION

### Fabrication and characterization of TBNCs@pDNA

The schematic representation of the synthesis process for TBNCs is depicted in Fig. 2A. This protocol, which is directed by proteins, uses amino acid residues of the PS to facilitate interaction and regulate the formation of clusters composed of AuPtCoPS. A series of TBNCs were fabricated by controlling the molar ratios of $HAuCl_4$, $H_2PtCl_6$, and $CoCl_2$ as 1:1:1, 2:1:2, 2:2:1, 1:2:2, 4:1:4, 4:4:1, and 1:4:4 (fig. S1A). Subsequently, the enzyme-like catalytic activities of TBNCs were examined by SOD and CAT activity assay kits, respectively. SOD is known for its ability to convert superoxide anion ($\bullet O^{2-}$) into oxygen ($O_2$) and $H_2O_2$, whereas CAT can break down $H_2O_2$ into $H_2O$ and $O_2$. The results indicate that the capacities for scavenging $\bullet O^{2-}$ and $H_2O_2$ differ among TBNCs with varying molar ratios. TBNCs cultured at a molar ratio of 2:1:2 exhibited the highest SOD activity, followed by TBNCs cultured at a molar ratio of 4:4:1 (fig. S1B). The highest CAT activity for TBNCs is achieved with the 1:4:4 molar ratio, followed by the 4:4:1 molar ratio (fig. S1C). Taken collectively, the optimal SOD and CAT activities of TBNCs can be achieved by maintaining a molar ratio of 4:4:1. Therefore, for subsequent experiments, the molar ratio of 4:4:1 was selected for the fabrication of TBNCs.

The morphology characterization of TBNCs was performed by high-resolution transmission electron microscopy (HRTEM) (Fig. 2, B to D), revealing a spherical shape with an average diameter of ~3.1 nm (Fig. 2C). Furthermore, the elemental mapping images illustrate a homogeneously alloyed nature of TBNCs, with the atomic fraction of Au, Pt, and Co being approximately 39:45:9 (fig. S2). Notably, the primary constituents of the PS compound were identified as phosphorus (P) and sulfur (S), indicating the successful formation of TBNCs within the protein matrix (Fig. 2D). In addition, the elemental composition and surface bonding of TBNCs were further investigated using x-ray photoelectron spectroscopy (XPS). (Fig. 2, E to H). The Au 4f spectrum exhibits two peaks at binding energies of approximately 83.4 and 87.1 eV, corresponding to the Au $4f_{7/2}$ and Au $4f_{5/2}$ spin states of zero-valent gold, respectively (Fig. 2F). The Pt 4f spectrum displays two peaks at 70.41 and 73.91 eV, which are associated with Pt $4f_{7/2}$ and Pt $4f_{5/2}$, respectively (Fig. 2G). During the nucleation process of trimetallic nanoparticles, PS attaches to metal nanoparticles via its cysteine residues,

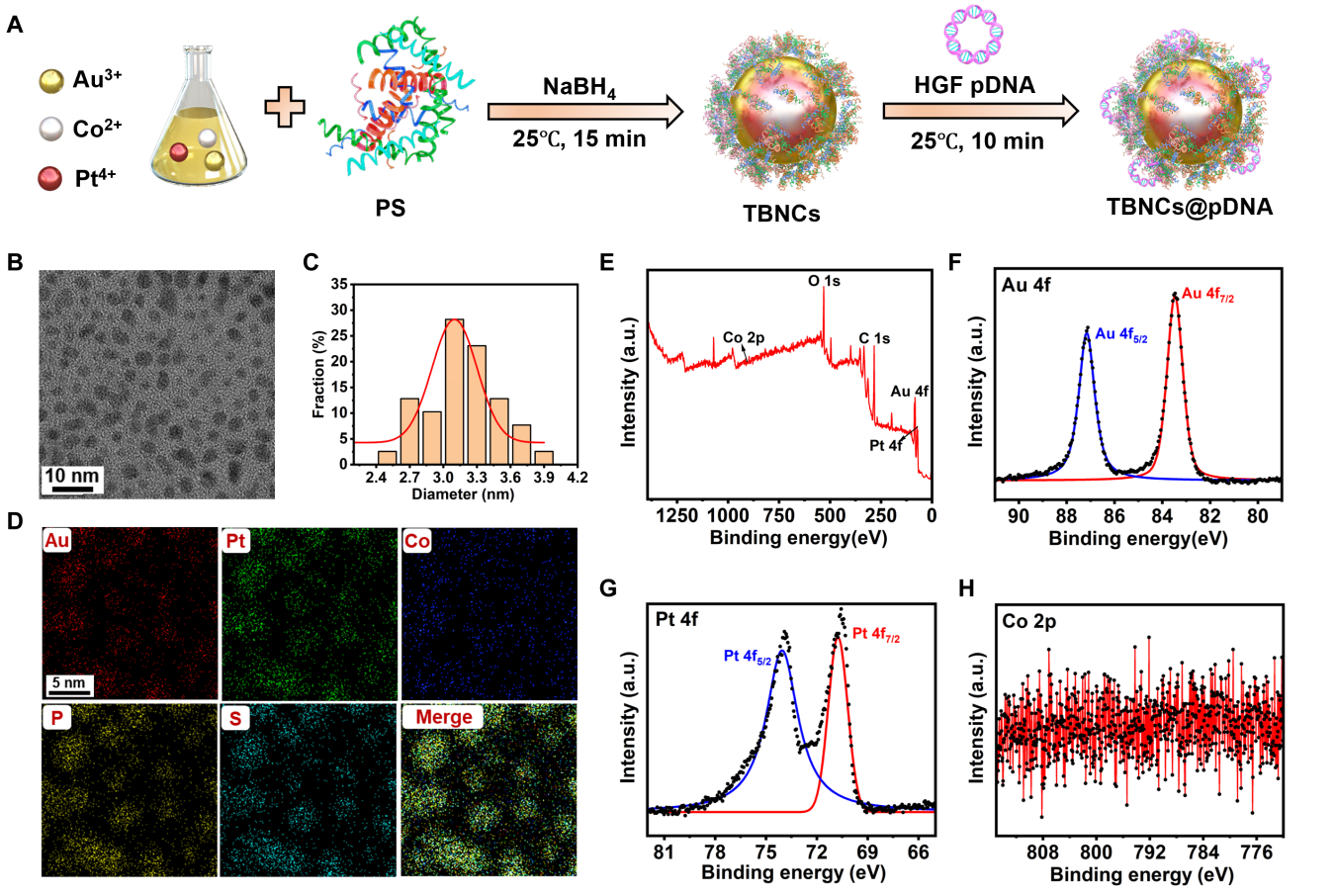


**Fig. 2. Synthesis, morphology characterization, and elemental analysis of TBNCs.** (**A**) Schematic illustration of the preparation of TBNCs. (**B**) Transmission electron microscopy (TEM) images of TBNCs and (**C**) the granulometric distribution. (**D**) Energy-dispersive x-ray spectroscopy mapping of Au, Pt, Co, P, and S elements for TBNCs. Scale bar, 5 nm. (**E**) X-ray photoelectron spectroscopy of TBNCs and the corresponding resolution spectrum for (**F**) Au 4f, (**G**) Pt 4f, and (**H**) Co 2p regions of TBNCs, respectively.

thereby imparting good stability to the nanoparticles (*33*). The decrease in binding energy values of Au $4f_{7/2}$ from 84.0 to 83.4 eV and Pt $4f_{7/2}$ from 71 to 70.41 eV, in comparison to the standard binding energy values of Au and Pt, further indicates a potential interaction between Au, Pt, and PS (*34*). Given that Co is predominantly distributed within the interior of TBNCs as opposed to being present on the surface, the XPS spectra for Co 2p do not exhibit a significant peak within the range of 770.0 to 810.0 eV (Fig. 2H).

The spin trap 5,5-dimethyl-1-pyrroline *N*-oxide (DMPO) as the probe in the electron paramagnetic resonance experiments allowed for the detection of oxygen-related radicals in the TBNCs reaction system. DMPO can capture the transient and highly reactive •HO and $•O^{2-}$ radicals, forming DMPO-•HO and DMPO-$•O^{2-}$ spin adducts, which exhibit characteristic spectra with intensity ratios of 1:2:2:1 and 1:1:1:1, respectively. The introduction of $Fe^{2+}$ and $H_2O_2$ led to the emergence of distinct spectral signals associated with the presence of •HO. However, the addition of TBNCs (58 μg/ml) effectively attenuated the spectral signal, thereby confirming the efficient elimination performance of TBNCs in eliminating •HO (Fig. 3B). Similarly, following the coincubation of xanthine with xanthine oxidase, unique peaks indicative of the presence of $•O^{2-}$ were observed. Upon the addition of TBNCs at a concentration of 19 μg/ml, a significantly attenuated characteristic peak became evident (Fig. 3C). All the results indicate that TBNCs exhibit remarkable SOD and CAT activities, enabling them to efficiently eliminate •HO and $•O^{2-}$ within the microenvironment (Fig. 3A). Hence, it is anticipated that the modification of MSCs with TBNCs will enhance their antioxidative stress capacity.

In addition to antioxidative stress capacity, the enhancement of the therapeutic efficacy of MSCs poses a critical and challenging issue in MSC-based therapy for IPF. Therefore, the delivery of HGF pDNA into MSCs was proposed as a strategy to augment their antifibrotic capabilities within the pathological IPF microenvironment. To achieve this, the HGF pDNA was initially designed and amplified, as illustrated in fig. S3. The pDNA loading efficiency of TBNCs was evaluated and optimized by agarose gel electrophoresis screening the ratio of TBNCs to pDNA (NPs:pDNA). The positive charges of TBNCs effectively counteracted the negative charges of pDNA, resulting in the inhibition of pDNA movement within the electric field, while the free pDNA exhibited unrestricted migration along the direction of the electric field within the gel. As evident from the results, as the weight ratio of TBNCs to pDNA increases, the bands

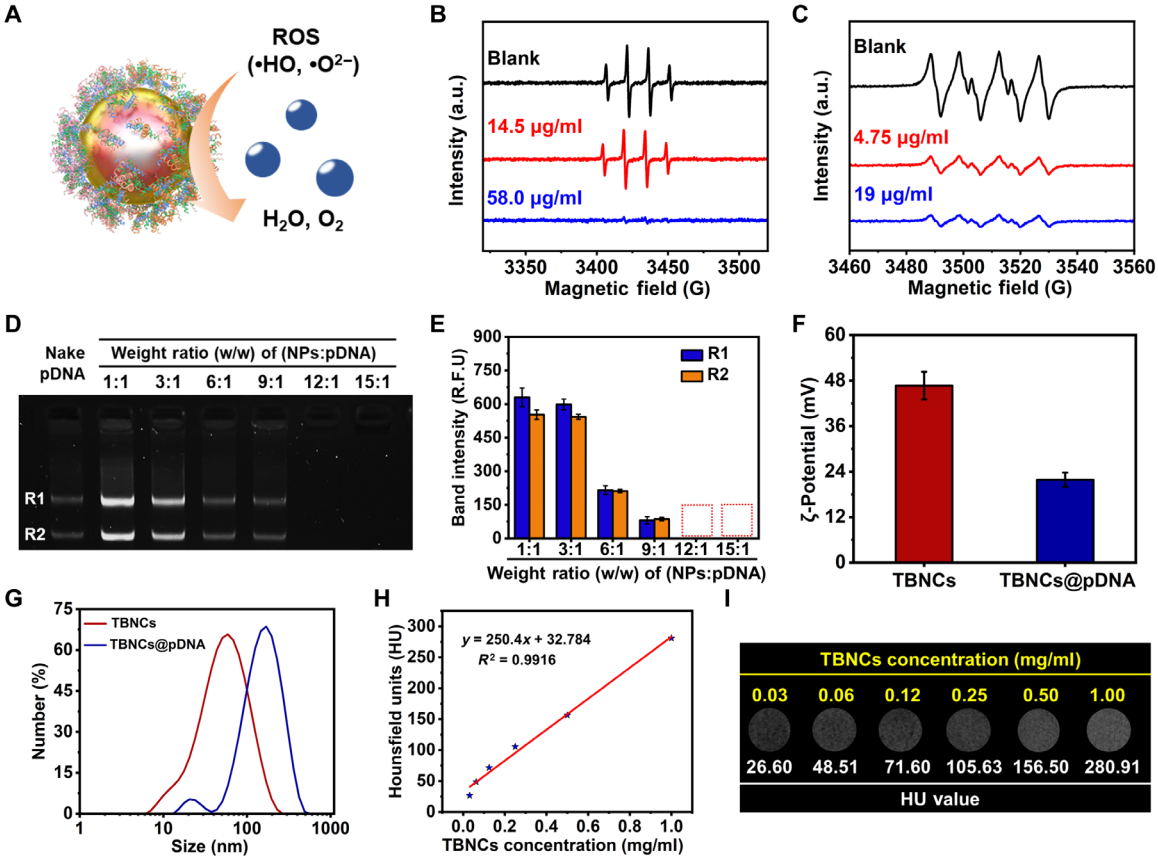


**Fig. 3. Enzyme-like activity, pDNA loading capacity, and CT imaging performance of TBNCs.** (**A**) Schematic illustration of enzyme-like activities of TBNCs. (**B**) Electron spin resonance (ESR) spectra of •HO generated by Fenton reaction with or without TBNC addition. (**C**) ESR spectra of $•O^{2-}$ generated by xanthine oxidase-xanthine system with or without TBNCs addition. a.u., arbitrary units. (**D**) Agarose gel electrophoresis of TBNCs/pDNA composites at different mass ratios of TBNCs to pDNA. Naked pDNA was taken as a control. (**E**) Electrophoretic band intensity at different mass ratios of TBNCs to pDNA. R.F.U., relative fluorescence unit. (**F**) Zeta potentials and (**G**) hydrodynamic diameters of TBNCs and TBNCs@pDNA, respectively. (**H**) Plot of Hounsfield unit (HU) values of TBNCs as a function of the concentration. (**I**) Transverse CT images of TBNCs at different concentrations. The value is expressed as the means ± SD, with a minimum sample size of 3.

of pDNA become narrower and completely vanish when the mass ratio of TBNCs to pDNA reaches 12:1, indicating that the optimal loading capacity of TBNCs for pDNA is achieved when the TBNCs:pDNA ratio is 12 (Fig. 3, D and E). The negatively charged HGF pDNA could be effectively adsorbed onto the positively charged surface of TBNCs, constructing a TBNCs@pDNA complex, which reduced the surface charge from 47 to 22 mV (Fig. 3F) and increased the hydrated particle size from 59 to 170 nm (Fig. 3G). Next, a high-resolution micro-CT system was used to evaluate the CT imaging performance of TBNCs@pDNA. With an increase in the concentration of TBNCs@pDNA, the CT images exhibited a progressive enhancement in luminosity, and the attenuation value exhibited a linear correlation with the TBNCs@pDNA content (Fig. 3, H and I), indicating that TBNCs@pDNA have a notable potential for CT imaging.

### TBNCs@pDNA-modified hMSCs exhibited favorable cell viability

The capacity of TBNCs@pDNA to label human MSCs (hMSCs) was investigated in the following experiment. To enhance the visualization of TBNCs@pDNA-labeled hMSCs, rhodamine B isothiocyanate (RBITC) was incorporated onto its surface, resulting in the creation of RB@TBNCs@pDNA. Subsequently, various concentrations of RB@TBNCs@pDNA (10, 20, 50, 100 μg/ml) were used in the incubation with hMSCs for 12 hours. The cellular labeling efficacy was assessed using laser confocal microscopy and flow cytometry. The results indicate that the intracellular fluorescence signal of hMSCs exhibited a gradual increase as the concentration of RB@TBNCs@pDNA incubation rose (Fig. 4A). The flow cytometry results also suggest that the fluorescence intensity of labeled cells increased with higher concentrations, although there was no substantial change in fluorescence intensity between 50 and 100 μg/ml (Fig. 4B). Then, hMSCs were coincubated with RB@TBNCs@pDNA (50 μg/ml) for 1, 2, 4, and 8 hours to evaluate the effectiveness of cell labeling with RB@TBNCs@pDNA over different incubation periods. Figure S4A depicts a modest rise in fluorescence intensity in the cytoplasm during the incubation period. The flow cytometry results indicate that the fluorescence intensity of labeled cells increases with longer incubation times, but the change becomes minimal after 4 hours (fig. S4B). In general, the optimal labeling concentration of 50 μg/ml and a duration of 4 hours can be distinctly chosen, leading to a cell labeling efficiency of more than 99% under these specified conditions (fig. S5). To enable the evaluation of the intracellular stability of TBNCs@pDNA, the RB@TBNCs@pDNA-labeled hMSCs were seeded onto all-black 96-well plates, with the medium being refreshed every 24 hours. The fluorescence intensity of the labeled hMSCs was measured at 24, 48, and 72 hours after inoculation. The results illustrated in fig. S6 indicate that there was no notable difference in fluorescence intensity observed between the 48-hour and 72-hour time points, indicating the stable presence of RB@TBNCs@pDNA within hMSCs cells.

The impact of TBNCs@pDNA on the functionality of hMSCs was evaluated through the use of a LIVE/DEAD staining kit. Calcein does not exhibit fluorescence in the presence of an obstructed calcium-binding site. Upon penetration of the cellular membrane and subsequent hydrolysis by metabolically active esterase in the cytoplasm, the compound exposes the calcium-binding site and establishes a bond with the calcium ion, leading to the manifestation of intense green fluorescence. The deceased cells, due to their inactive esterase, do not display green fluorescence, but they are marked with propidium iodide (PI) as a result of compromised membrane selectivity, leading to red fluorescence. Consequently, the levels of red and green fluorescences emitted by cells can serve as reliable indicators of cell viability. As illustrated in Fig. 4C, the cells exhibit intense green fluorescence and minimal red fluorescence, indicating a high level of activity. During the initial phase of apoptosis, there is a translocation of phosphatidylserine from the inner leaflet to the outer leaflet of the lipid membrane (*35*). Annexin V exhibits a high affinity for phosphatidylserine, interacts with it, and subsequently binds to the cell membrane. This characteristic makes annexin V a sensitive marker for the detection of early apoptosis. The utilization of fluorescein isothiocyanate (FITC)–labeled annexin V as a fluorescent probe in conjunction with PI, a nucleic acid dye that is unable to permeate intact cell membranes, distinguished early apoptotic cells from late-stage and nonviable cells. The findings from flow cytometry indicate that the cell viability remains at or above 90% even when subjected to an incubation concentration of 100 μg/ml (Fig. 4D). Next, the proliferation potential of the TBNCs@pDNA-labeled cells was investigated. The results demonstrated that the rate of cellular healing was approximately 13.67% on the initial day after inoculation, and it increased to around 85.41% by the fourth day, which indicated that the cells' ability to proliferate was not substantially affected and remained robust (fig. S7).

The stemness of hMSCs, that is, the ability to self-renew and differentiate into multiple downstream cell types (*36*), forms the foundation for treating IPF. We thus investigated the differentiation potential of TBNCs@pDNA-labeled hMSCs into two downstream cellular lines, namely, adipocytes and osteoblasts (*37*). TBNCs@pDNA were coincubated with hMSCs, and once the cell healing degree reached 75 to 80%, the cells were subsequently exposed to lipogenic and osteogenic induction differentiation medium for 14 and 28 days, respectively. Following solidification of the cells with 4% paraformaldehyde, they underwent staining with Oil Red O dye and alizarin red dye, leading to the observation of distinct lipid droplets and calcium nodules indicating that the TBNCs@pDNA did not exert a significant influence on the stemness of hMSCs (fig. S8, A and B).

### Gene delivery efficiency and in vitro CT imaging of the labeled hMSCs

To assess the effectiveness of TBNCs@pDNA in delivering HGF plasmid to cells, hMSCs were cultured in a serum-free environment and coincubated with TBNCs@pDNA for 24 hours. The choice to use serum-free culture was based on the propensity of serum to create a protein layer on the surface of nanoparticles, which hinders their cellular uptake (*38*, *39*). The HGF pDNA primarily encompasses the genetic sequence for the enhanced green fluorescent protein (EGFP) and the HGF. The utilization of laser confocal microscopy allowed for the distinct observation of green fluorescence emitted by EGFP, indicating the effective internalization of the HGF pDNA by cells and its subsequent integration into the nucleus to facilitate gene expression. To further validate these findings, the expression of HGF was specifically detected using immunofluorescence techniques. The revealed results indicated a clear colocalization of the red fluorescence signal of HGF and the green fluorescence signal of EGFP, providing further confirmation of the successful expression of HGF (Fig. 4E). In addition, the quantification of HGF expression in TBNCs@pDNA-labeled hMSCs was

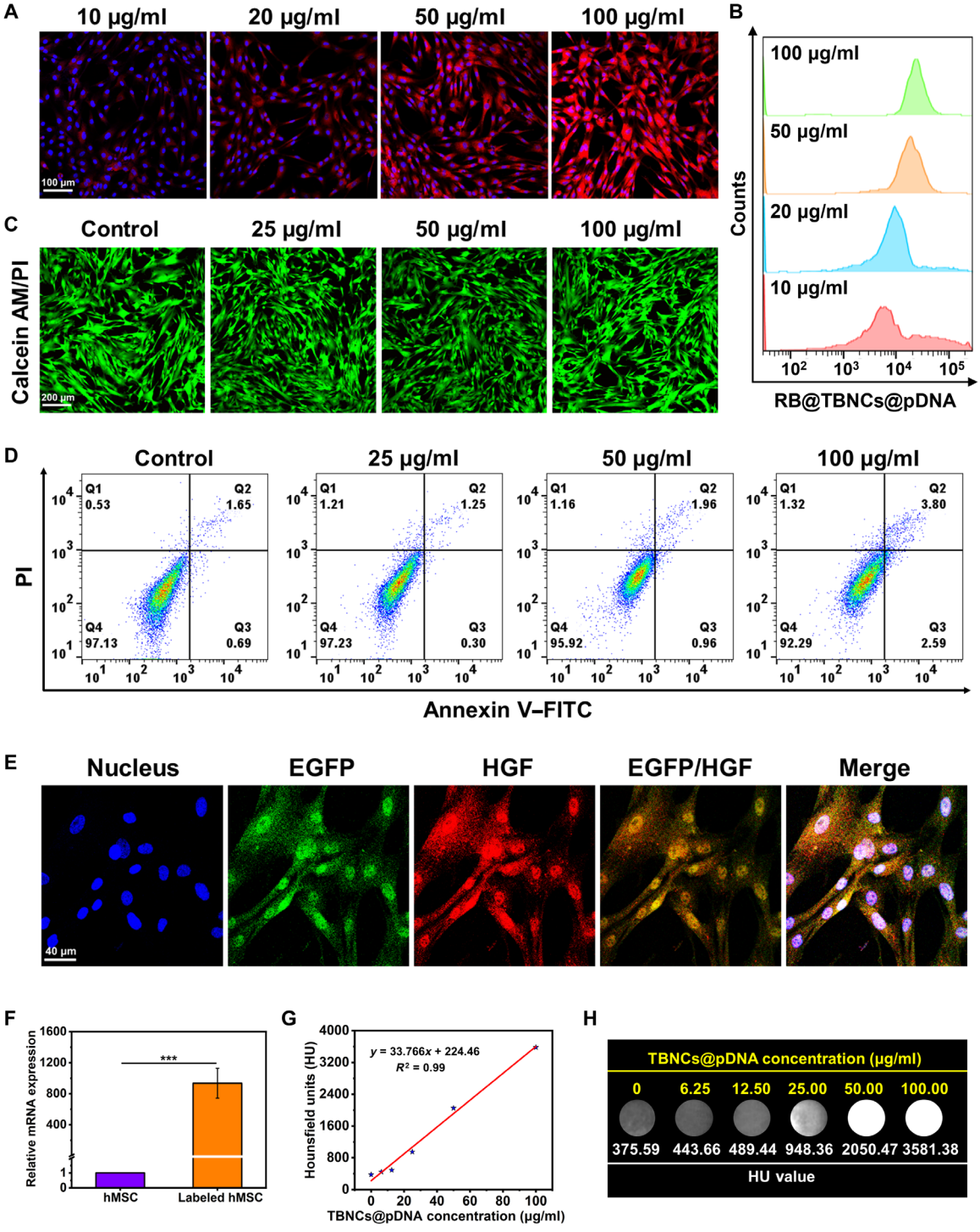


**Fig. 4. Cell labeling ability and gene delivery ability of TBNCs@pDNA and CT imaging performance of their labeled hMSCs.** (**A**) Laser confocal microscopy images of the hMSCs labeled with TBNCs@pDNA at different concentrations; blue and red fluorescences stand for the nucleus stained with 4′,6-diamidino-2-phenylindole (DAPI) and the TBNCs@pDNA-labeled hMSCs, respectively. (**B**) Flow cytometry analysis of the hMSCs labeled with TBNCs@pDNA at different concentrations. (**C**) Live/dead staining of hMSCs after being treated with TBNCs@pDNA at different concentrations. Red and green fluorescences stand for the dead hMSCs stained with propidium iodide (PI) and alive hMSCs stained with calcein AM. (**D**) Flow cytometry analysis of the apoptosis of hMSCs with or without TBNCs@pDNA at different concentrations. (**E**) Immunofluorescence analysis of HGF expression in the hMSCs labeled with TBNCs@pDNA. Red: HGF, Green: EGFP, Blue: DAPI-stained nucleus. (**F**) Quantification of reverse transcription quantitative polymerase chain reaction data of HGF expression in the hMSCs labeled with TBNCs@pDNA. (**G**) Calculated HU values as a function of the concentration of TBNCs@pDNA added for cell labeling, and (**H**) in vitro CT images of the hMSCs labeled with TBNCs@pDNA at different concentrations. The symbol *** indicates a statistically significant difference at $P < 0.001$. The value is expressed as the means ± SD, with a minimum sample size of 3.

conducted through reverse transcription polymerase chain reaction. The level of HGF expression in labeled hMSCs was determined to be 935 times greater than in unlabeled hMSCs (Fig. 4F). Transfecting hMSCs is widely recognized as a challenging undertaking (*40*). However, in this study, the efficient delivery and successful expression of the HGF pDNA into the hMSCs were achieved, attributed to the remarkable cell membrane translocation and specific nuclear-targeting capability of PS.

The in vitro CT imaging performance of hMSCs labeled with TBNCs@pDNA is essential for enabling the effective real-time tracking of labeled hMSCs in vivo, so the CT imaging potential of labeled hMSCs was evaluated using micro-CT. Compared to unlabeled hMSCs at 375.59 Hounsfield units (HU), hMSCs labeled with TBNCs@pDNA exhibited a notable attenuation in attenuation on micro-CT imaging. The cells labeled with concentrations of 6.25, 12.5, 25, 50, and 100 μg/ml exhibited 443.66, 489.44, 948.36, 2050.47, and 3581.38 HU, respectively (Fig. 4H), showing a linear relationship between the attenuation and the quantity of TBNCs@pDNA added for labeling (Fig. 4G). The sensitivity of CT detection for TBNCs@pDNA-labeled hMSCs was assessed. In our experiment, hMSCs were initially labeled with TBNCs@pDNA (50 μg/ml). Subsequently, they were suspended in 1% agarose at various cell numbers per tube (25 μl). As illustrated in fig. S9, the CT values were determined as 643.94, 672.49, 720.28, 769.23, and 901.52 HU for $1.625 \times 10^5$, $3.25 \times 10^5$, $6.5 \times 10^5$, $1.25 \times 10^6$, and $2.5 \times 10^6$ cells, respectively. In comparison to agarose alone (613.64 HU), the labeled hMSCs exhibited a prominent signal on CT imaging, with the detection limit estimated to be approximately $3.25 \times 10^5$ cells.

### TBNCs@pDNA protect hMSCs from intracellular oxidative damage

The main factor to be considered in maintaining the viability of hMSCs in fibrotic lung tissue is their ability to withstand the effects of ROS following transplantation (*21*, *22*). Subsequently, a cellular model of $H_2O_2$-induced oxidative stress was used in vitro to evaluate the efficacy of TBNCs in eliminating intracellular ROS. The fluorescent probe 2,7-dichlorodihydrofluorescein diacetate (DCFH-DA) is used for the detection of ROS in a cellular model. DCFH-DA does not exhibit inherent fluorescence and can permeate the cellular membrane for intracellular esterase-mediated hydrolysis, resulting in the production of DCFH. DCFH accumulates within the cell over time due to its inability to permeate the cell membrane. Intracellular ROS have the capacity to oxidize non-fluorescent DCFH, leading to the generation of green fluorescent 2,7-dichlorofluorescein (DCF), and the fluorescence intensity may serve as an indicator of the intracellular ROS level (*41*). As illustrated in Fig. 5A, following $H_2O_2$ stimulation, the cytoplasm of hMSCs exhibits intense green fluorescence, whereas the cytoplasmic fluorescence of TBNC-labeled hMSCs is significantly reduced, indicating that TBNCs have a strong capacity to eliminate ROS. Notably, the presence of ROS has had a reduction in hMSC viability to 66%, while the successful removal of ROS from TBNCs has led to an increase in cell viability to 90% (Fig. 5B).

The mitochondria serve as the central hub for cellular life processes, governing not only the cell's respiratory chain and oxidative phosphorylation but also the regulation of apoptosis. Following the invasion of exogenous ROS in hMSCs, the mitochondria of hMSCs will exhibit a stress response. Briefly, the ROS triggers the opening of the mitochondrial permeability transition pore, leading to the liberation of calcium ions, cytochrome C, and apoptosis-inducing factors. This process initiates the activation of caspase-9, which subsequently induces the activation of caspase-3/6/7, leading to a decrease in adenine nucleoside triphosphate production and an increase in the expression of pro-apoptotic proteins, ultimately disintegrating the outer membrane of mitochondria and apoptosis (*42*, *43*). The mitochondrial morphology and structure of hMSCs after ROS invasion were investigated using biological TEM. The results revealed that the mitochondria of TBNCs@pDNA-labeled hMSCs exhibited a similar rod-like or globular structure to that of normal hMSCs, even when subjected to ROS attack. Conversely, after being exposed to a ROS attack, there was an increase in the mitochondrial volume of hMSCs, leading to a more rounded shape. In addition, the mitochondrial matrix became faint or transparent, the mitochondrial ridge shortened or disappeared, and the interridge cavity expanded (Fig. 5C). The aforementioned phenomenon suggests that the mitochondria of unlabeled hMSCs experienced notable damage following invasion by ROS, whereas the mitochondria of labeled hMSCs remained comparatively undamaged. Next, the apoptosis of hMSCs resulting from mitochondrial damage was monitored. According to the results of flow cytometry analysis, 20.6% of hMSCs were in late apoptosis and 13.6% were in necrosis after ROS invasion, while the proportions of hMSCs labeled with TBNCs@pDNA in late apoptosis and necrosis decreased to 7.66 and 2.59%, respectively (Fig. 5D). In short, the TBNCs@pDNA demonstrate the capacity to effectively enhance the resistance of hMSCs to oxidative stress caused by ROS, thereby helping to prevent mitochondrial structural damage, and ultimately are expected to improve the survival rate of hMSCs in fibrotic lung conditions.

### The labeled hMSCs have therapeutic efficacy in vitro

During the early stages of IPF, there is an up-regulation in the production of pulmonary inflammatory factors and the occurrence of endoplasmic reticulum stress in AECs, leading to the impairment of AECs and the degradation of the alveolar basement membrane (*44*). As a result, enhancing the repair of AECs can effectively ameliorate compromised alveolar function and impede the progression of IPF. The repair effects of TBNCs@pDNA-labeled hMSCs on injured AECs were evaluated in a wound-healing assay. Bronchial epithelium transformed with Ad12-SV40 2B (BEAS 2B) cells with scratches was cultured in normal medium (control group), hMSC-conditioned medium (hMSC-CM group), and TBNCs@pDNA-labeled hMSC-conditioned medium (labeled hMSC-CM group), respectively. The process of wound healing was observed using an inverted microscope, and the area of the scratch before and after repair was analyzed statistically. The results demonstrate that the healing degree of BEAS 2B cells in the labeled hMSC-CM group was notably higher than that in the other groups after 24 hours of culture, with the hMSC-CM following closely (Fig. 6, A and C). The enhanced capacity of BEAS 2B cells for repairing damage when exposed to labeled hMSC-CM culture can be ascribed to the overexpression of HGF in the labeled hMSCs, leading to the stimulation of proliferation and migration in BEAS 2B cells, as well as the inhibition of apoptosis.

Upon experiencing recurrent injury, the AECs undergo a phenotypic transition to myofibroblasts in response to activating agents like transforming growth factor β1 (TGF-β1), which further stimulates the expression of fibrotic markers such as α–smooth muscle actin (α-SMA), collagen I (Col I), and fibronectin (FN), a phenomenon referred to as epithelial-mesenchymal transformation (EMT)

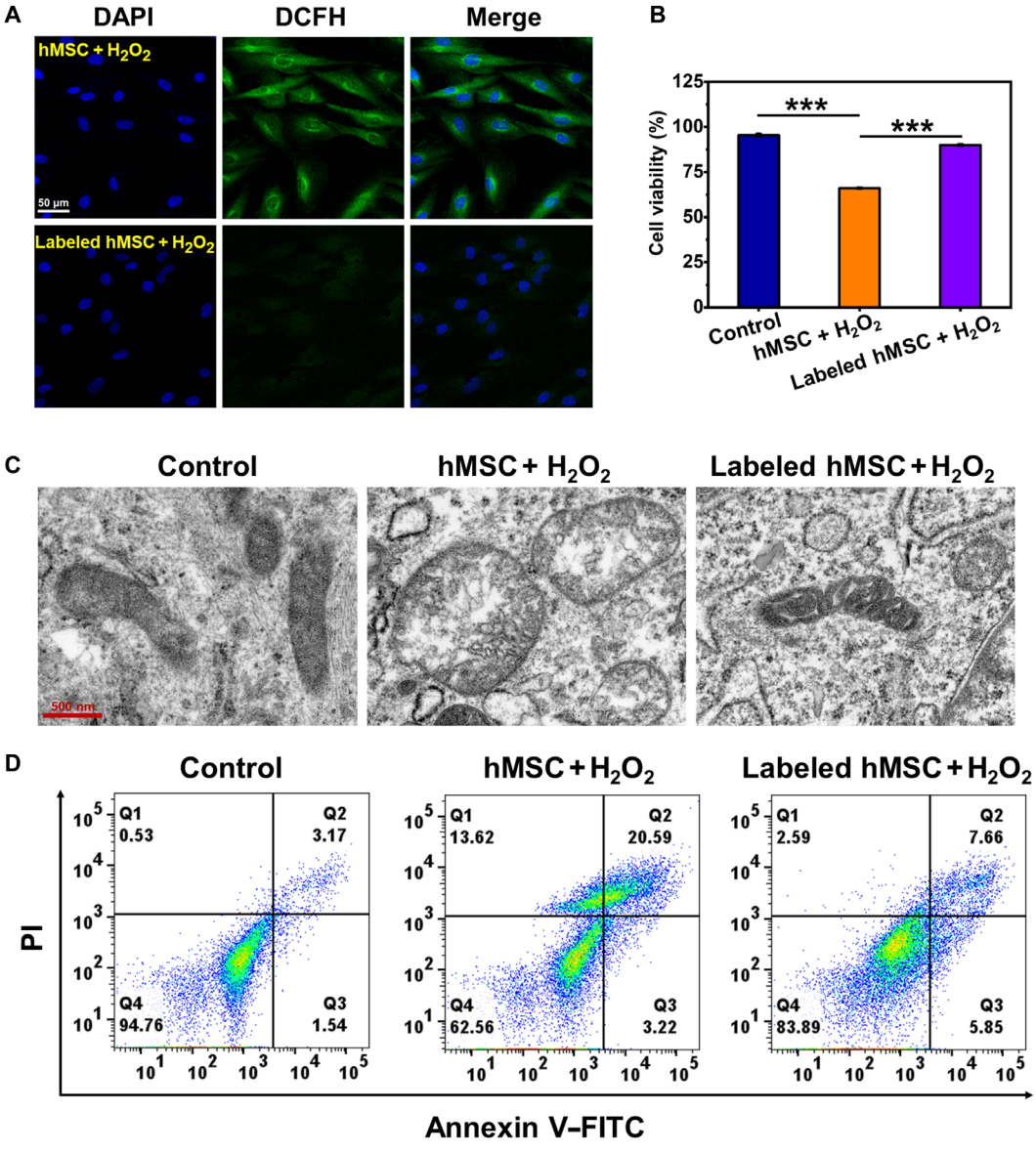


**Fig. 5. Assessment of the intracellular antioxidative stress capacity of TBNCs in hMSCs.** (**A**) Intracellular generation of ROS following $H_2O_2$ stimulation. Significant ROS generation, indicated by green fluorescence, was observed in pure hMSCs, and (**B**) the cell viability of hMSCs and hMSCs labeled with TBNCs following exposure to $H_2O_2$ stimulation. (**C**) TEM images of mitochondrial structure and morphology of hMSCs and hMSCs labeled with TBNCs after $H_2O_2$ stimulation. (**D**) Flow cytometry analysis of the apoptosis of hMSCs and hMSCs labeled with TBNCs before and after $H_2O_2$ stimulation. The symbol *** indicates a statistically significant difference at $P < 0.001$. The value is expressed as the means ± SD, with a minimum sample size of 3.

(*45*). In this study, TGF-β1 was used to prompt the differentiation of BEAS 2B cells into myofibroblasts, mimicking the development of pulmonary fibrosis in vivo. The BEAS-2B cells were subjected to exposure to TGF-β1, hMSC-CM + TGF-β1, and labeled hMSC-CM + TGF-β1 for a duration of 24 hours. Subsequently, the cellular expressions of fibrosis markers α-SMA, FN, and Col I were detected using the immunofluorescence technique, and the mean fluorescence intensity was quantitatively assessed using ImageJ software (Fig. 6, B and D to F). The up-regulation of α-SMA, FN, and Col I was significantly induced by TGF-β1, while hMSC-CM and labeled hMSC-CM notably attenuated the expression of these three fibrosis markers, with labeled hMSC-CM demonstrating the most significant inhibition. These results further indicate that HGF suppresses the signaling of TGF-β1 and the transition of the AECs into myofibroblasts. This phenomenon can be elucidated by the ability of HGF to stimulate the generation of TGF-β1 signaling inhibitors, such as Smad7 expression, through a mechanism dependent on mitogen-activated protein kinase, which is expected to hinder the transformation of AECs into myofibroblasts, thereby impeding the progression of pulmonary fibrosis (*46*).

Myofibroblasts are significantly involved in the pathogenesis of IPF by secreting a substantial amount of ECM that accumulates in the lung interstitium, leading to the collapse of alveolar structure and impairing gas exchange function, and ultimately contributing

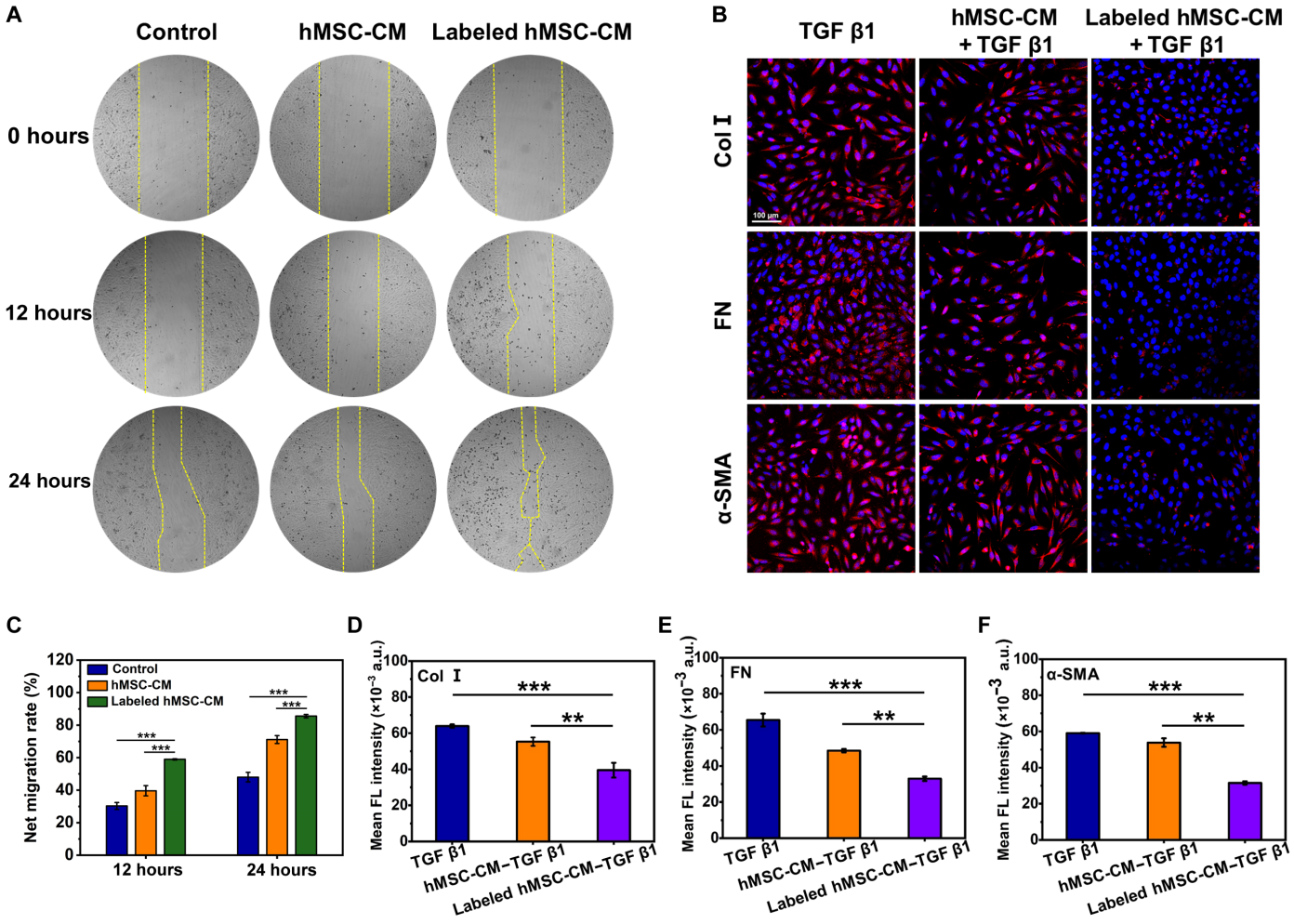


**Fig. 6. Evaluation of the capacity of hMSCs labeled with TBNCs to facilitate the repair of damaged BEAS 2B and to impede the transformation of AECs into myofibroblasts in vitro.** (**A**) Representative images of BEAS 2B wound-healing assays treated with normal medium, hMSC-CM, or labeled hMSC-CM for 12 and 24 hours. (**B**) Representative images of collagen I (Col I; red), α–smooth muscle actin (α-SMA; red), and fibronectin (FN; red) immunostaining of BEAS 2B after treatment with transforming growth factor β1 (TGF-β1), hMSC-CM + TGF-β1, and labeled hMSC-CM + TGF-β1, respectively. The nuclei were stained with DAPI (blue). (**C**) The net migration rate of BEAS 2B per well. Quantification of (**D**) Col I, (**E**) FN, and (**F**) α-SMA staining after treatment. The symbols ** and *** indicate a statistically significant difference at $P < 0.01$ and $P < 0.001$, respectively. The value is expressed as the means ± SD, with a minimum sample size of 3.

to the mortality of patients with respiratory failure (*47*). Hence, the induction of myofibroblast apoptosis, along with the reduction or degradation of ECM accumulation in the lung interstitium, plays a crucial role in inhibiting or potentially reversing the progression of IPF. Subsequently, the capacity of TBNCs@pDNA-engineered hMSCs to stimulate apoptosis in myofibroblasts was assessed. Myofibroblasts were cultured with normal medium, hMSC-CM, and labeled hMSC-CM for 24 hours, respectively. The apoptosis of myofibroblasts was assessed using the annexin V–FITC/PI staining kit. Fluorescence microscope images revealed that the labeled hMSC-CM led to a notable increase in myofibroblasts apoptosis, as evidenced by the increased annexin V–FITC and PI-positive signals, in comparison to the hMSC-CM and normal medium groups. While the hMSC-CM group also exhibited positive staining for annexin V–FITC and PI, the signal intensity was significantly lower compared to the labeled hMSC-CM group (fig. S10A). The obtained results were in line with those derived from flow cytometry analysis. Upon exposure to labeled hMSC-CM, the myofibroblasts exhibited a mortality rate of 50.3%, which was three times greater than that of the control group in normal medium (15.5%) and two times higher than that of the group exposed to hMSC-CM (22.4%) (fig. S10B). Previous studies have shown that matrix metalloproteinase 2 (MMP-2) and MMP-9 are capable of degrading a range of collagen, gelatin, and basement membranes within the cellular interstitium. Moreover, MMP-2 and MMP-9 have been observed to trigger apoptosis in myofibroblasts, indicating their potential as candidates for antifibrotic interventions (*48*). The c-Met protein operates as a receptor tyrosine kinase and fulfills the role of a receptor for HGF, thereby initiating the HGF/c-Met signal transduction pathway. Upon activation, the signal transduction system has the capability to up-regulate the expression of MMP-2 and MMP-9 in myofibroblasts, thereby initiating the apoptosis pathway of myofibroblasts (*49*). Hence, we used the enzyme-linked immunosorbent assay to measure the levels of MMP-2 and MMP-9 expression during the

apoptosis of myofibroblasts triggered by labeled hMSC-CM, and the results indicated that the labeled hMSC-CM resulted in elevated levels of active MMP-2 and MMP-9 in the supernatants of myofibroblasts. Notably, the augmentation of MMP-9 levels induced by labeled hMSC-CM was more pronounced compared to the effect observed on MMP-2 levels (fig. S11).

Understanding the mechanisms of IPF is crucial for the development of effective prevention and treatment strategies. Nevertheless, the precise mechanism of IPF has not been completely elucidated. The onset of IPF starts with the damage and aberrant regeneration of AECs, culminating in the induction of EMT, which promotes the transformation of AECs into myofibroblasts. Myofibroblasts are responsible for the secretion of a significant quantity of ECM, which accumulates in the lung interstitium, ultimately resulting in the collapse of the alveolar structure. The TBNCs@pDNA-engineered hMSCs in this study exhibited the capacity to effectively regenerate damaged AECs, suppress EMT, and induce apoptosis of myofibroblasts, which is expected to significantly hinder the progression of IPF.

### In vivo dual-modal imaging tracking of the labeled hMSCs

To monitor the viability of transplanted hMSCs in vivo, we initially established an hMSCs line ($hMSCs^{luc}$) with a consistent expression of the luciferase (Luc) reporter gene through lentiviral transfection (fig. S12). Subsequently, TBNCs@pDNA were coincubated with $hMSCs^{luc}$ to obtain the labeled $hMSCs^{luc}$. The biosafety of labeled $hMSCs^{luc}$ was examined before their transplantation into IPF mice. The results indicate that TBNCs@pDNA could be rapidly metabolized by the metabolic system, and the Au amounts in the lung tissue decreased from 55 to 13 μg after 45 days of transplantation (fig. S13). Moreover, the labeled $hMSCs^{luc}$ were injected in situ into normal mice, and the major organs of the mice were subsequently removed 2 months later for pathological analysis. The findings indicated that the heart, liver, spleen, lungs, and kidneys of the experimental mice did not exhibit any abnormal pathological alterations in comparison to those of the control group (fig. S14). Next, bleomycin (BLM) was administered directly into the lungs to induce the up-regulation of fibrosis-related genes, activate associated pathways, and mimic the process of fibrosis, thereby establishing a murine model of IPF. Initially, the IPF mice underwent characterization through micro-CT imaging. The findings from the two-dimensional (2D) image analysis indicated that the lungs of IPF mice exhibited grid-like alterations and irregular expansion of peripheral bronchial branches. The density of the diseased tissue was evaluated through the analysis of the alterations in the mean CT value, allowing for a quantitative assessment of the scope and severity of pulmonary fibrosis. The 3D image analysis revealed a restricted quantity of functional ventilation sites in IPF mice, accounting for only 16% of the normal aeration zone, leading to the mice suffering from severe respiratory failure (Fig. 7, A and B). Furthermore, the pathological results of Masson's trichrome staining and hematoxylin and eosin staining reveal notable collagen accumulation in the lung interstitium of IPF mice, along with severe impairment of the alveolar structure (Fig. 7C). Thus, all results validated the successful establishment of a murine model for pulmonary fibrosis.

Following the transplantation of the labeled $hMSCs^{luc}$ trachea into IPF mice, the in vivo viability of the transplanted hMSCs was monitored in real time using the IVIS Lumina II system. On the third day after transplantation, there was an increase in lung bioluminescence (BL) intensity from $3.94 \times 10^5$ photons per second (p/s) to $4.83 \times 10^5$ p/s, potentially indicating a rapid proliferation of hMSCs within the initial 3-day period following transplantation. From day 5 onward, there was a gradual decrease in the intensity of the BL, accompanied by an accelerated rate of decline. This phenomenon may be associated with a decreased rate of proliferation of hMSCs in comparison to the rate of apoptosis, the latter of which demonstrates a gradual increase. Moreover, it was noted that while the overall BL intensity decreased on the seventh day, the peak BL intensity surpassed that of the fifth day ($41.79 \times 10^2$ p/s), reaching $48.22 \times 10^2$ p/s, which may be caused by the migration of hMSCs or the specific stimulation of the injured site to facilitate hMSCs proliferation. Compared with previous studies, we modified hMSCs with TBNCs@pDNA to enhance their resilience to pulmonary oxidative stress and significantly promoted the survival rate of hMSCs in mice with IPF, effectively prolonging their survival from 7 to 14 days (Fig. 7, D to F) (*50*–*52*). However, the survival of transplanted hMSCs in the lungs of IPF mice is influenced not only by oxidative stress but also by additional factors including hypoxia and inadequate nutrient delivery. Hence, it is imperative to persist in optimizing the strategy to tackle the challenge of the low lung survival rate of hMSCs in IPF mice.

The real-time visualization of the biological behavior, such as distribution, migration, and homing of transplanted hMSCs in mice with IPF, is advantageous for optimizing hMSC therapy and for timely monitoring of its efficacy. However, the resolution of BL imaging is constrained, making it challenging to observe the distribution and migration of transplanted hMSCs in vivo. Consequently, micro-CT imaging was used in vivo to observe the biological behavior of transplanted hMSCs. After transplantations of labeled hMSCs into IPF mice, the presence of hMSCs (yellow color) was detected in the upper lung (red color) region (Fig. 8B). Real-time CT images acquired from three horizontal layers indicate that the CT signals from hMSCs are predominantly located in two areas, denoted by yellow and red arrows, respectively. The three horizontal layers represent cross sections from the top to the bottom of the lung. As depicted in Fig. 8A, the CT signal area at the yellow arrow of layer 1 exhibited a gradual decrease over time until it nearly vanished, while the CT value increased on the 5th and 10th day. This phenomenon may be attributed to the migration of hMSCs to the fibrotic injury site. Our previous study also substantiated the ability of hMSCs to migrate to the fibrotic site (*20*). Furthermore, it is evident that there was a substantial decrease in the CT signal intensity and area at the red mark of layer 1 on the fifth day, while the CT signal area at the red mark of layers 2 and 3 increased, indicating that hMSCs possibly migrated from layer 1 to layers 2 and 3 on the fifth day. When combined with 3D CT images, hMSCs exhibited proliferation on the fifth day, with the signal area gradually decreasing over time. Consequently, the comprehensive distribution, migration, and other biological activities of hMSCs in the management of pulmonary fibrosis can be observed, allowing for real-time visualization of the effectiveness of hMSCs in treating pulmonary fibrosis, which will facilitate the technical optimization of hMSC-based therapy (Fig. 8, C to E). While the BL imaging results indicated that transplanted hMSCs survived for up to 14 days in IPF mice, a 45-day observation was conducted to explore the long-term tracer ability of TBNCs@pDNA. It was observed that the CT signal gradually diminished over time, but the distribution of hMSCs remained clearly visible on the 45th day (fig. S15). Therefore, it also established a basis for

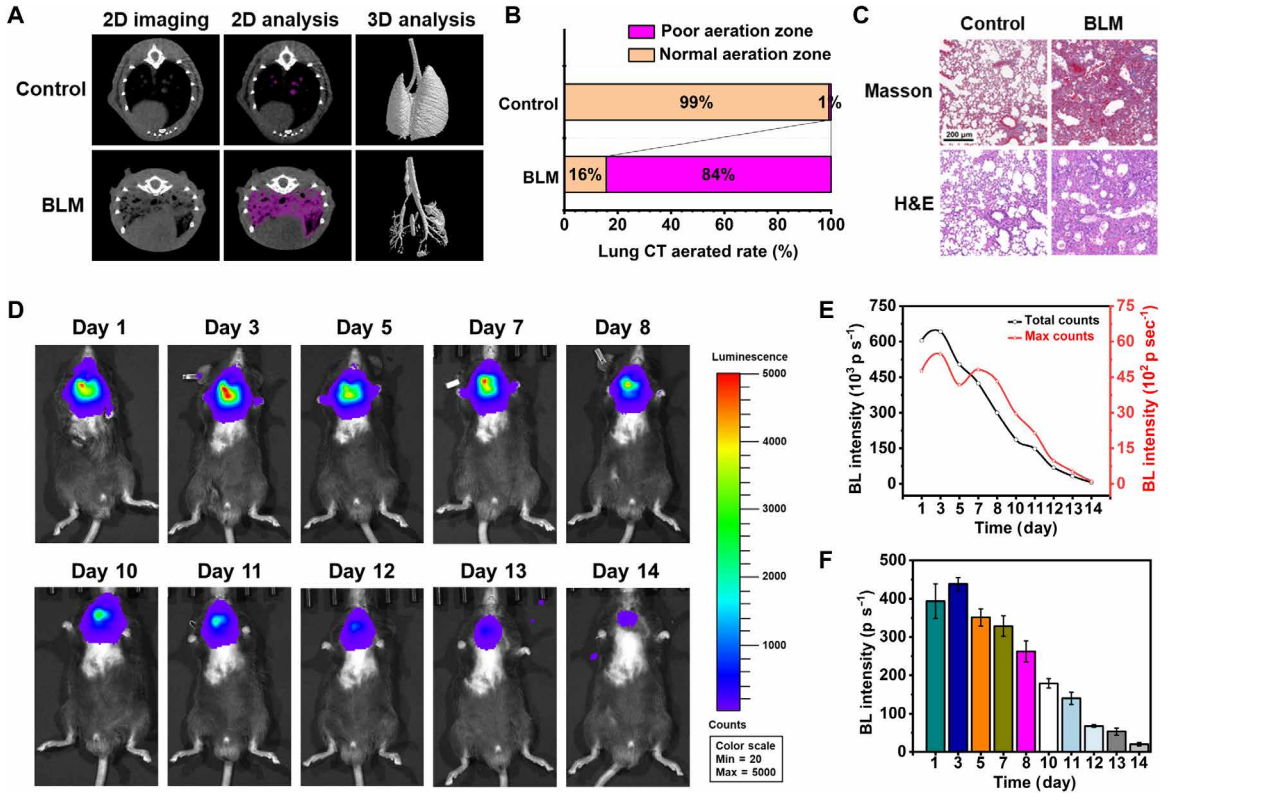


**Fig. 7. Construction of IPF model and visualization of the survival state of TBNC-labeled hMSCs transplanted into IPF mice.** (**A**) Micro-CT images of mice with and without bleomycin (BLM) injection after 21 days and (**B**) the percentages of pulmonary CT ventilation ratio. (**C**) Lung sections from the control and BLM groups were stained using hematoxylin and eosin (H&E) and Masson's trichrome staining techniques. (**D**) BL images of the TBNC-labeled hMSCs at various time intervals in IPF mice. (**E**) Quantitative statistics of the difference between the total BL intensity and the maximum BL intensity. (**F**) Quantitative statistics pertaining to the mean BL intensity. The value is expressed as the means ± SD, with a minimum sample size of 3.

achieving the long-term tracking of transplanted hMSCs. To confirm whether the TBNCs still stayed in the labeled hMSCs after transplantation, the lung tissue was taken out for sectioning 45 days after transplantation. TBNCs@pDNA was pre-tagged with RBITC, and the cytomembrane dye 3,3′-dioctadecyloxacarbocyanine perchlorate (DiO) was used to mark hMSCs before transplantation. The laser confocal microscopy images displayed that the red fluorescence region (RB@TBNCs@pDNA) matched well with the green fluorescence region (DiO-hMSCs), distinctly demonstrating the presence of TBNCs in the labeled hMSCs. Consequently, it is clear that the imaging signals were the true signals of the labeled cells (fig. S16). Collectively, the hMSCs labeled with TBNCs@pDNA could be tracked for 45 days via CT after transplantation in the lung.

## The labeled hMSCs have therapeutic efficacy in vivo

Next, the therapeutic effect of labeled hMSCs on IPF in vivo was evaluated. The study first involved the detection of HGF expression levels in labeled hMSCs within fibrotic lungs using specific immunofluorescence staining. As illustrated in Fig. 9A, labeled hMSCs exhibit a pronounced expression of HGF in the lungs of mice with IPF, with the level of expression significantly exceeding that of the other experimental groups. In addition, it was also observed that mice injected with BLM exhibited elevated expression of HGF in their pulmonary tissue. Although the expression level was not higher than that of mice transplanted with hMSCs, it was notably higher than that of the control group (Fig. 9B). This discovery is consistent with our previous assertions: When exposed to BLM stimulation, the interstitial cells of mice lungs exhibit a significant increase in HGF expression, which aids in the restoration of damaged AECs (*19*, *53*, *54*). Subsequently, the expression of α-SMA and Col I, which serve as markers of pulmonary fibrosis was examined. The results suggested that labeled hMSCs were capable of significantly reducing the expression levels of both factors, exhibiting a notably higher efficiency in down-regulation compared to unlabeled hMSCs (Fig. 9, C to F). We speculate that the observed phenomenon was linked to the heightened expression of HGF by labeled hMSCs, which effectively facilitated the restoration of lung epithelial cells, suppressed EMT, and stimulated the apoptosis of myofibroblasts, thereby reducing the levels of α-SMA and Col I at the site of action. The involvement of the NLRP3 inflammasome in BLM-induced EMT suggests that evaluating the NLRP3 expression level can offer valuable insights into the degree of inhibition of EMT (*55*). Terminal deoxynucleotidyl transferase–mediated deoxyuridine triphosphate nick end labeling (TUNEL) can be used to assess the apoptosis of myofibroblasts. Hence, we examined the expression levels of NLRP3 and α-SMA in lung tissues pre- and postlabeled hMSCs transplantation through paraffin tissue immunohistochemistry. In addition, we assessed the apoptosis of myofibroblasts using

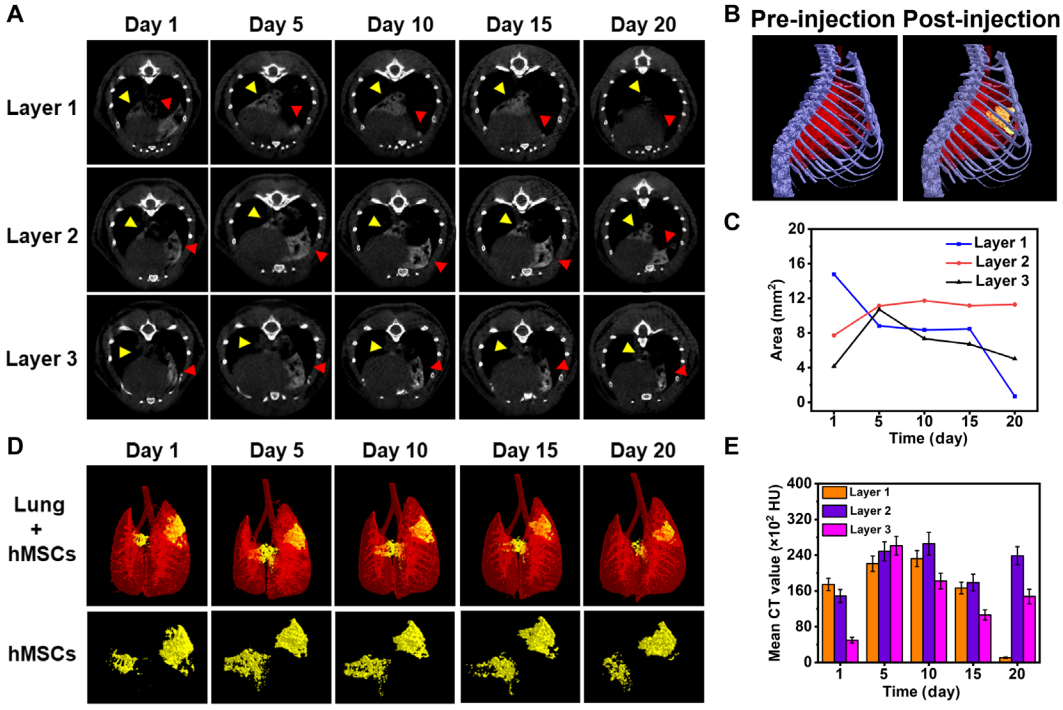


**Fig. 8. Visualization of biological behavior of TBNC-labeled hMSCs transplanted into IPF mice.** (**A**) In vivo micro-CT images (indicated by yellow and red arrows) of the labeled hMSCs at 1, 5, 10, 15, and 20 days after transplantation into the lung of IPF mice, respectively. (**B**) 3D in vivo CT images of the labeled hMSCs in IPF mice before (left) and after (right) transplantation. (**C**) Graph illustrating the distribution area of CT signals from labeled hMSCs in relation to the duration of transplantation. (**D**) 3D CT images depict the labeled hMSCs at 1, 5, 10, 15, and 20 days after transplantation into the lung of IPF mice. (**E**) CT values of the labeled hMSCs after transplantation into the lung at different time points. The value is expressed as the means ± SD, with a minimum sample size of 3.

TUNEL staining. The findings indicated that the transplantation of labeled hMSCs markedly suppressed the expression of NLRP3 (fig. S17A), suggesting that labeled hMSCs have the potential to effectively impede EMT and hinder the advancement of pulmonary fibrosis. Furthermore, the expression of α-SMA was decreased in the group treated with transplanted labeled hMSCs (fig. S17B), and there was a notable increase in the number of positive cells in the TUNEL staining results of the transplanted labeled hMSCs treatment group (fig. S17C), indicating that transplanted labeled hMSCs have the potential to effectively induce apoptosis of myofibroblasts. This result is consistent with the outcomes of our in vitro experiments.

Subsequent detection of structural alterations occurred in the lung tissue of IPF mice both before and following the application of labeled hMSCs therapy. Micro-CT imaging was used to identify scarring in the lung tissue of mice in the BLM group, characterized by an accumulation of excess fibrous connective tissue that compressed the alveoli, leading to alveolar collapse and reducing oxygen supply to the blood (Fig. 10A). It is postulated that the diminished survival rate of transplanted hMSCs in the lungs of mice with IPF may also be related to the reduced oxygen supply following fibrotic lesions. In addition, pathological analysis of lung tissue revealed a substantial deposition of collagen in the lung interstitium of the BLM group, resulting in dense scars and honeycomb-like changes due to alveolar collapse. Nevertheless, despite the presence of similar pathological changes in the labeled hMSCs group, the overall preservation of lung tissue structure seemed to be superior in comparison to the other groups (Fig. 10B and fig. S18). In addition, the 2D and 3D CT imaging results indicate a notable reduction in the normal aeration area of the lung in the BLM group, which demonstrates notable improvement after treatment with labeled hMSCs (Fig. 10A). The degree of lung aeration in mice that were administered labeled hMSCs was determined to be as high as 96%, a significantly greater level compared to the unlabeled hMSCs group (75%) and the BLM group (44%) (Fig. 10, C to E).

In general, hMSCs engineered with TBNCs@pDNA demonstrate the ability to effectively withstand oxidative stress in fibrotic lungs and notably enhance their in vivo survival rate. Simultaneously, engineered hMSCs exhibited a high level of HGF expression at the fibrotic site, actively facilitating the repair of damaged lung epithelial cells, reducing the expression of Col I and α-SMA, thereby impeding the progression of pulmonary fibrosis and fostering the structural reorganization of lung tissue.

In summary, TBNCs have been synthesized by a simple and reliable method, showcasing remarkable enzyme-like activity, effective gene delivery, and exceptional potential for CT imaging. First, TBNCs effectively eradicate ROS in transplanted hMSCs, thereby enhancing their viability and extending the lifespan of transplanted hMSCs in vivo to 14 days. Second, TBNCs efficiently deliver HGF pDNA into hMSCs, leading to a 935-fold increase in HGF expression and ultimately enhancing the antifibrotic potential of transplanted hMSCs. In addition, integration of the robust CT imaging attributes of TBNCs with the bioluminescence capacities of hMSCs that constitutively express luciferase enables the real-time monitoring

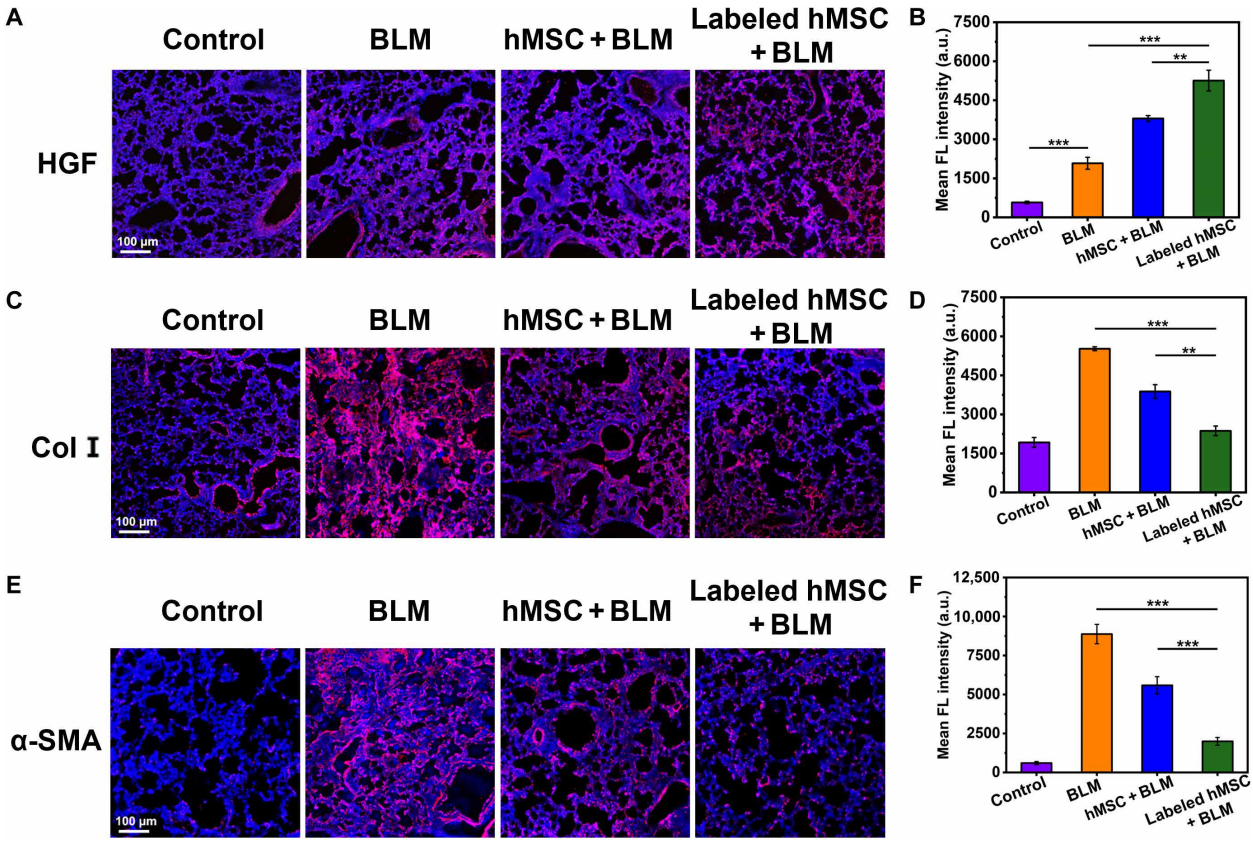


**Fig. 9. Expression of HGF and fibrosis markers Col I and α-SMA in the lung of IPF mice.** (**A**) Laser confocal microscopy images and (**B**) fluorescence intensity of the expression of HGF in the lung tissue of IPF mice treated with hMSC and labeled hMSC, respectively. Laser confocal microscopy images and corresponding fluorescence intensity of the expressions of (**C** and **D**) Col I and (**E** and **F**) α-SMA in the lung tissue of IPF mice treated with hMSC and labeled hMSC, respectively. The untreated and BLM-treated mice were used as negative and positive controls, respectively. The symbols ** and *** indicate a statistically significant difference at $P < 0.01$ and $P < 0.001$, respectively. The value is expressed as the means ± SD, with a minimum sample size of 3.

of the in vivo distribution, migration, and viability of transplanted hMSCs. This approach enhances comprehension of the mechanisms by which transplanted MSCs for treating IPF and contributes to the optimization of techniques in MSC-based therapy. Consequently, this study presents a previously unidentified approach for engineering MSCs to endow therapeutic and imaging capabilities, to lay the crucial technical groundwork for advancing clinical research and streamlining the large-scale production of high-quality MSCs in the realm of regenerative medicine.

## MATERIALS AND METHODS

### Study design

The purpose of this study was to use TBNCs loaded with HGF pDNA to genetically engineer hMSCs to enhance their antioxidative stress and antifibrosis capabilities. Simultaneously, the biological behaviors, including distribution, migration, and survival of transplanted hMSCs in vivo, were real-time visualized in CT/BL dual-modal imaging. To achieve this objective, PS was initially used as the template protein for the one-step synthesis of TBNCs. Next, the activities of SOD and CAT enzymes, the pDNA loading capacity, and the CT imaging performance of TBNCs were assessed and optimized.

Second, we examined the in vitro cell labeling, gene delivery, and antioxidant stress capabilities of TBNCs@pDNA. TBNCs@pDNA-labeled hMSCs have been shown to efficiently express HGF pDNA, resulting in a 935-fold increase in expression level. In addition, TBNCs@pDNA efficiently eliminate ROS in hMSCs and enhance the survival rate to more than 90%. The antifibrotic potential of TBNCs@pDNA-labeled hMSCs was assessed in vitro, with a focus on their capacity to repair injured lung epithelial cells, inhibit epithelial-mesenchymal transition, and induce apoptosis of myofibroblasts. Furthermore, it was also verified that the TBNCs@pDNA-labeled hMSCs exhibited favorable performance in CT imaging in vitro.

Third, the therapeutic effect of labeled hMSCs on IPF was investigated in vivo. Initially, BLM was administered to C57BL/6 mice to induce pulmonary fibrosis and establish an IPF model. Simultaneously, the lentivirus transfection technique was used to establish constitutive hMSCs expressing the luciferase reporter gene ($hMSCs^{luc}$) to monitor the survival status of transplanted hMSCs in vivo. Subsequently, TBNCs@pDNA-labeled $hMSCs^{luc}$ were transplanted into the lungs of IPF mice via tracheal transplantation. The distribution, migration, survival, and efficacy of the transplanted hMSCs were visualized in vivo using CT imaging combined with BL imaging. In addition, lung tissues were promptly extracted for

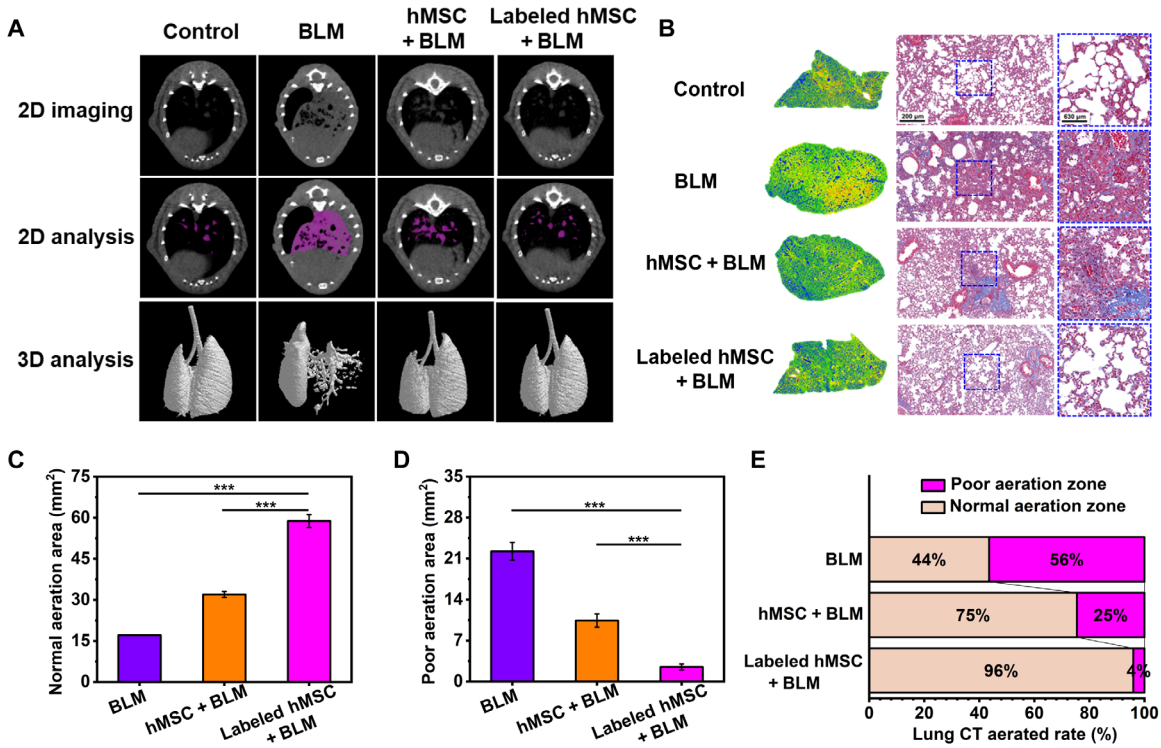


**Fig. 10. Efficacy of TBNC-labeled hMSCs in the treatment of pulmonary fibrosis in vivo.** (**A**) Micro-CT images of the IPF mice treated with hMSC or labeled hMSC and (**B**) Masson's trichrome staining of the lung tissues from the IPF mice treated with hMSC or labeled hMSC. The untreated mouse served as the negative control, while the BLM-treated mouse served as the positive control. (**C**) The normal aeration area and (**D**) the poor aeration area were compared between the hMSC- and labeled hMSC–treated groups and the untreated groups. (**E**) The percentages of pulmonary CT ventilation ratio were compared between the hMSC- and labeled hMSC–treated groups and the untreated groups. The symbol *** denotes a statistically significant difference at a significance level of $P < 0.001$. The value is expressed as the means ± SD, with a minimum sample size of 3.

pathological examination and, in conjunction with the findings from CT imaging and immunohistochemical staining, the effects of transplanted hMSCs on the inhibition of fibrosis and the promotion of lung tissue remodeling in IPF mice were assessed.

All animal experiments were carried out in compliance with the approved protocol of the Regional Ethics Committee for Animal Experiments of Ningbo University, China [permit no. (Zhe) 2019-0005]. The determination of sample size is established through reference to published literature to guarantee statistical significance. Data files S1 and S2 contain comprehensive information regarding the sample size, statistical analysis, and experimental design, along with accompanying charts and legends.

### Statistical analysis

All statistical data were shown as means ± SEM. Correlation between groups was evaluated using Student's *t* test. Differences were considered significant at $*P < 0.05$, $**P < 0.01$, and $***P < 0.001$.

## Supplementary Materials

**This PDF file includes:**

Supplementary Materials and Methods
Figs. S1 to S18
Table S1
Legends for data files S1 and S2
References

**Other Supplementary Material for this manuscript includes the following:**

Data files S1 and S2

## REFERENCES AND NOTES

1. A. J. Podolanczuk, C. C. Thomson, M. Remy-Jardin, L. Richeldi, F. J. Martinez, M. Kolb, G. Raghu, Idiopathic pulmonary fibrosis: State of the art for 2023. *Eur. Respir. J.* **61**, 2200957 (2023).
2. R. J. Allen, J. M. Oldham, D. A. Jenkins, O. C. Leavy, B. Guillen-Guio, C. A. Melbourne, S.-F. Ma, J. Jou, J. S. Kim; Clean UP-IPF Investigators of the Pulmonary Trials Cooperative, W. A. Fahy, E. Oballa, R. B. Hubbard, V. Navaratnam, R. Braybrooke, G. Saini, K. M. Roach, M. D. Tobin, N. Hirani, M. K. B. Whyte, N. Kaminski, Y. Zhang, F. J. Martinez, A. L. Linderholm, A. Adegunsoye, M. E. Strek, T. M. Maher, P. L. Molyneaux, C. Flores, I. Noth, R. Gisli Jenkins, L. V. Wain, Longitudinal lung function and gas transfer in individuals with idiopathic pulmonary fibrosis: A genome-wide association study. *Lancet Respir. Med.* **11**, 65–73 (2023).
3. J. C. Hewlett, J. A. Kropski, T. S. Blackwell, Idiopathic pulmonary fibrosis: Epithelial-mesenchymal interactions and emerging therapeutic targets. *Matrix Biol.* **71–72**, 112–127 (2018).
4. M. Myllarniemi, R. Kaarteenaho, Pharmacological treatment of idiopathic pulmonary fibrosis-preclinical and clinical studies of pirfenidone, nintedanib, and N-acetylcysteine. *Eur. Clin. Respir. J.* **2**, 26385 (2015).
5. T. M. Dempsey, V. Thao, D. A. Helfinstine Jr., Y. H. Chang, L. Sangaralingham, A. H. Limper, Real-world cohort evaluation of the impact of the antifibrotics in patients with idiopathic pulmonary fibrosis. *Eur. Respir. J.* **62**, doi.org/10.1183/13993003.01299-2023 (2023).
6. O. Burgy, A. A. Mailleux, ATAC-ing single nucleus in idiopathic pulmonary fibrosis: TWIST1 strives back for myofibroblasts. *Eur. Respir. J.* **62**, doi.org/10.1183/13993003.00881-2023 (2023).
7. J. Liang, Y. Zhang, T. Xie, N. Liu, H. Chen, Y. Geng, A. Kurkciyan, J. M. Mena, B. R. Stripp, D. Jiang, P. W. Noble, Hyaluronan and TLR4 promote surfactant-protein-C-positive

alveolar progenitor cell renewal and prevent severe pulmonary fibrosis in mice. *Nat. Med.* **22**, 1285–1293 (2016).
8. R. L. Toonkel, J. M. Hare, M. A. Matthay, M. K. Glassberg, Mesenchymal stem cells and idiopathic pulmonary fibrosis. Potential for clinical testing. *Am. J. Respir. Crit. Care Med.* **188**, 133–140 (2013).
9. E. E. Agha, R. Kramann, R. K. Schneider, X. Li, W. Seeger, B. D. Humphreys, S. Bellusci, Mesenchymal stem cells in fibrotic disease. *Cell Stem Cell* **21**, 166–177 (2017).
10. L. A. Ortiz, F. Gambelli, C. McBride, D. Gaupp, M. Baddoo, N. Kaminski, D. G. Phinney, Mesenchymal stem cell engraftment in lung is enhanced in response to bleomycin exposure and ameliorates its fibrotic effects. *Proc. Natl. Acad. Sci. U.S.A.* **100**, 8407–8411 (2003).
11. A. Averyanov, I. Koroleva, M. Konoplyannikov, V. Revkova, V. Lesnyak, V. Kalsin, O. Danilevskaya, A. Nikitin, A. Sotnikova, S. Kotova, V. Baklaushev, First-in-human high-cumulative-dose stem cell therapy in idiopathic pulmonary fibrosis with rapid lung function decline. *Stem Cells Transl. Med.* **9**, 6–16 (2020).
12. A. Campo, J. M. González-Ruiz, E. Andreu, A. B. Alcaide, M. M. Ocón, J. De-Torres, J. Pueyo, R. Cordovilla, E. Villaron, F. Sanchez-Guijo, M. Barrueco, J. Nuñez-Córdoba, F. Prósper, J. J. Zulueta, Endobronchial autologous bone marrow-mesenchymal stromal cells in idiopathic pulmonary fibrosis: A phase I trial. *ERJ Open Res.* **7**, doi.org/10.1183/23120541.00773-2020 (2021).
13. M. M. Han, X. Y. He, L. Tang, L. Qi, M. Y. Yang, Y. Wang, L. Xing, J. H. Jeong, H. L. Jiang, Nanoengineered mesenchymal stem cell therapy for pulmonary fibrosis in young and aged mice. *Sci. Adv.* **9**, eadg5358 (2023).
14. H. Zhou, Y. Zhang, P. Pei, W. Shen, X. Yi, K. Yang, Liposome-anchored mesenchymal stem cells for radiation pneumonia/fibrosis treatment. *Biomaterials* **300**, 122202 (2023).
15. S. H. Kim, H. H. Moon, H. A. Kim, K. C. Hwang, M. Lee, D. Choi, Hypoxia-inducible vascular endothelial growth factor-engineered mesenchymal stem cells prevent myocardial ischemic injury. *Mol. Ther.* **19**, 741–750 (2011).
16. H. Chen, Y. Luo, Y. Zhu, Y. Ye, D. Chen, X. Song, Z. Xiao, M. Liu, S. Li, Enhanced secretion of hepatocyte growth factor in human umbilical cord mesenchymal stem cells ameliorates pulmonary fibrosis induced by bleomycin in rats. *Front. Pharmacol.* **13**, 1070736 (2023).
17. B. Crestani, S. Marchand-Adam, C. Quesnel, L. Plantier, K. Borensztajn, J. Marchal, A. Mailleux, P. Soler, M. Dehoux, Hepatocyte growth factor and lung fibrosis. *Proc. Am. Thorac. Soc.* **9**, 158–163 (2012).
18. A. Gazdhar, P. Fachinger, C. van Leer, J. Pierog, M. Gugger, R. Friis, R. A. Schmid, T. Geiser, Gene transfer of hepatocyte growth factor by electroporation reduces bleomycin-induced lung fibrosis. *Am. J. Physiol. Lung Cell. Mol. Physiol.* **292**, L529–L536 (2007).
19. H. Bao, Y. Li, C. Yu, X. Li, Y. Wang, L. Gao, J. Huang, Z. Zhang, DNA-coated gold nanoparticles for tracking hepatocyte growth factor secreted by transplanted mesenchymal stem cells in pulmonary fibrosis therapy. *Biomater. Sci.* **10**, 368–375 (2022).
20. H. Bao, S. Cheng, X. Li, Y. Li, C. Yu, J. Huang, Z. Zhang, Functional Au nanoparticles for engineering and long-term CT imaging tracking of mesenchymal stem cells in idiopathic pulmonary fibrosis treatment. *Biomaterials* **288**, 121731 (2022).
21. A. L. Mora, M. Rojas, A. Pardo, M. Selman, Emerging therapies for idiopathic pulmonary fibrosis, a progressive age-related disease. *Nat. Rev. Drug Discov.* **16**, 755–772 (2017).
22. L. Guo, G. Karoubi, P. Duchesneau, F. G. Aoki, M. V. Shutova, I. Rogers, A. Nagy, T. K. Waddell, Interrupted reprogramming of alveolar type II cells induces progenitor-like cells that ameliorate pulmonary fibrosis. *NPJ Regen. Med.* **3**, 14 (2018).
23. T. H. Yang, J. Ahn, S. Shi, P. Wang, R. Gao, D. Qin, Noble-metal nanoframes and their catalytic applications. *Chem. Rev.* **121**, 796–833 (2021).
24. N. Liao, L. Su, Y. Cao, L. Qiu, R. Xie, F. Peng, Z. Cai, X. Liu, J. Song, Y. Zeng, Tracking cell viability for adipose-derived mesenchymal stem cell-based therapy by quantitative fluorescence imaging in the second near-infrared window. *ACS Nano* **16**, 2889–2900 (2022).
25. G. Chen, Y. Zhang, C. Li, D. Huang, Q. Wang, Q. Wang, Recent advances in tracking the transplanted stem cells using near-infrared fluorescent nanoprobes: Turning from the first to the second near-infrared window. *Adv. Healthc. Mater.* **7**, e1800497 (2018).
26. K. S. Dhada, D. S. Hernandez, L. J. Suggs, In vivo photoacoustic tracking of mesenchymal stem cell viability. *ACS Nano* **13**, 7791–7799 (2019).
27. C. Liu, J. Xing, O. U. Akakuru, L. J. Luo, S. Sun, R. F. Zou, Z. S. Yu, Q. L. Fang, A. G. Wu, Nanozymes-engineered metal-organic frameworks for catalytic cascades-enhanced synergistic cancer therapy. *Nano Lett.* **19**, 5674–5682 (2019).
28. O. U. Akakuru, C. Xu, C. Liu, Z. Li, J. Xing, C. Pan, Y. Li, E. I. Nosike, Z. Zhang, Z. M. Iqbal, J. Zheng, A. Wu, Metal-free organo-theranostic nanosystem with high nitroxide stability and loading for image-guided targeted tumor therapy. *ACS Nano* **15**, 3079–3097 (2021).
29. A. El-Sayed, S. Futaki, H. Harashima, Delivery of macromolecules using arginine-rich cell-penetrating peptides: Ways to overcome endosomal entrapment. *AAPS J.* **11**, 13–22 (2009).
30. F. Pei, S. Feng, Y. Zhang, Y. Wu, C. Chen, Y. Sun, Z. Xie, Q. Hao, Y. Cao, Z. Tong, W. Lei, A photoelectrochemical immunosensor based on Z-scheme CdS composite heterojunction for aflatoxin B1. *Biosens. Bioelectron.* **214**, 114500 (2022).
31. Q. Wang, H. Wei, Z. Zhang, E. Wang, S. Dong, Nanozyme: An emerging alternative to natural enzyme for biosensing and immunoassay. *Trends Analyt. Chem.* **105**, 218–224 (2018).
32. S. Cai, J. Liu, J. Ding, Z. Fu, H. Li, Y. Xiong, Z. Lian, R. Yang, C. Chen, Tumor-microenvironment-responsive cascade reactions by a cobalt-single-atom nanozyme for synergistic nanocatalytic chemotherapy. *Angew. Chem. Int. Ed. Engl.* **61**, e202204502 (2022).
33. H. Zhu, Z. Pan, E. W. Hagaman, C. Liang, S. H. Overbury, S. Dai, Facile one-pot synthesis of gold nanoparticles stabilized with bifunctional amino/siloxy ligands. *J. Colloid Interface Sci.* **287**, 360–365 (2005).
34. D. Shcharbin, E. Pedziwiatr-Werbicka, T. Serchenya, S. Cyboran-Mikolajczyk, L. Prakhira, V. Abashkin, V. Dzmitruk, M. Ionov, S. Loznikova, I. Shyrochyna, O. Sviridov, C. E. Peña-González, A. B. Gumiel, R. Gómez, F. J. de la Mata, M. Bryszewska, Role of cationic carbosilane dendrons and metallic core of functionalized gold nanoparticles in their interaction with human serum albumin. *Int. J. Biol. Macromol.* **118**, 1773–1780 (2018).
35. S. Nagata, J. Suzuki, K. Segawa, T. Fujii, Exposure of phosphatidylserine on the cell surface. *Cell Death Differ.* **23**, 952–961 (2016).
36. D. M. Hoang, P. T. Pham, T. Q. Bach, A. T. L. Ngo, Q. T. Nguyen, T. T. K. Phan, G. H. Nguyen, P. T. T. Le, V. T. Hoang, N. R. Forsyth, M. Heke, L. T. Nguyen, Stem cell-based therapy for human diseases. *Signal Transduct. Target. Ther.* **7**, 272 (2022).
37. T. Kim, J. E. Lemaster, F. Chen, J. Li, J. V. Jokerst, Photoacoustic imaging of human mesenchymal stem cells labeled with prussian blue-poly(L-lysine) nanocomplexes. *ACS Nano* **11**, 9022–9032 (2017).
38. Y. Qiu, Y. Liu, L. Wang, L. Xu, R. Bai, Y. Ji, X. Wu, Y. Zhao, Y. Li, C. Chen, Surface chemistry and aspect ratio mediated cellular uptake of Au nanorods. *Biomaterials* **31**, 7606–7619 (2010).
39. B. D. Chithrani, W. C. W. Chan, Elucidating the mechanism of cellular uptake and removal of protein-coated gold nanoparticles of different sizes and shapes. *Nano Lett.* **7**, 1542–1550 (2007).
40. J. Sunshine, J. J. Green, K. P. Mahon, F. Yang, A. A. Eltoukhy, D. N. Nguyen, R. Langer, D. G. Anderson, Small-molecule end-groups of linear polymer determine cell-type gene-delivery efficacy. *Adv. Mater.* **21**, 4947–4951 (2009).
41. C. Rota, C. F. Chignell, R. P. Mason, Evidence for free radical formation during the oxidation of 2′-7′-dichlorofluorescin to the fluorescent dye 2′-7′-dichlorofluorescein by horseradish peroxidase: Possible implications for oxidative stress measurements. *Free Radic. Biol. Med.* **27**, 873–881 (1999).
42. S. Márquez-Jurado, J. Díaz-Colunga, R. P. das Neves, A. Martinez-Lorente, F. Almazán, R. Guantes, F. J. Iborra, Mitochondrial levels determine variability in cell death by modulating apoptotic gene expression. *Nat. Commun.* **9**, 389 (2018).
43. Y. Lu, Z. Li, L. Li, J. Chen, X. Xu, Z. Lin, T. Zhang, Y. Zhu, C. Ding, C. Mao, Highly effective rheumatoid arthritis therapy by peptide-promoted nanomodification of mesenchymal stem cells. *Biomaterials* **283**, 121474 (2022).
44. Z. Borok, M. Horie, P. Flodby, H. Wang, Y. Liu, S. Ganesh, A. L. Firth, P. Minoo, C. Li, M. F. Beers, A. S. Lee, B. Zhou, Grp78 loss in epithelial progenitors reveals an age-linked role for endoplasmic reticulum stress in pulmonary fibrosis. *Am. J. Respir. Crit. Care Med.* **201**, 198–211 (2020).
45. N. Khalil, O. Bereznay, M. Sporn, A. H. Greenberg, Macrophage production of transforming growth factor beta and fibroblast collagen synthesis in chronic pulmonary inflammation. *J. Exp. Med.* **170**, 727–737 (1989).
46. M. N. Shukla, J. L. Rose, R. Ray, K. L. Lathrop, A. Ray, P. Ray, Hepatocyte growth factor inhibits epithelial to myofibroblast transition in lung cells via Smad7. *Am. J. Respir. Cell Mol. Biol.* **40**, 643–653 (2009).
47. A. V. Misharin, G. R. S. Budinger, Targeting the myofibroblast in pulmonary fibrosis. *Am. J. Respir. Crit. Care Med.* **198**, 834–835 (2018).
48. T. Bormann, R. Maus, J. Stolper, M. Tort Tarrés, C. Brandenberger, D. Wedekind, D. Jonigk, T. Welte, J. Gauldie, M. Kolb, U. A. Maus, Role of matrix metalloprotease-2 and MMP-9 in experimental lung fibrosis in mice. *Respir. Res.* **23**, 180 (2022).
49. J. Jung, K. Yang, H. J. Kim, Y. J. Lee, M. Kim, Y. H. Choi, J. L. Kang, RhoA-dependent HGF and c-Met mediate Gas6-induced inhibition of epithelial-mesenchymal transition, migration, and invasion of lung alveolar epithelial cells. *Biomolecules* **9**, 565 (2019).
50. H. Bao, Y. Xia, C. Yu, X. Ning, X. Liu, H. Fu, Z. Chen, J. Huang, Z. Zhang, CT/Bioluminescence dual-modal imaging tracking of mesenchymal stem cells in pulmonary fibrosis. *Small* **15**, e1904314 (2019).
51. C. Yu, Y. Lv, X. Li, H. Bao, X. Cao, J. Huang, Z. Zhang, SOD-functionalized gold nanoparticles as ROS scavenger and CT contrast agent for protection and imaging tracking of mesenchymal stem cells in idiopathic pulmonary fibrosis treatment. *Chem. Eng. J.* **459**, doi.org/10.1016/j.cej.2023.141603 (2023).
52. Y. Lv, C. Yu, X. Li, H. Bao, S. Song, X. Cao, H. Lin, J. Huang, Z. Zhang, ROS-activatable nanocomposites for CT imaging tracking and antioxidative protection of mesenchymal stem cells in idiopathic pulmonary fibrosis therapy. *J. Control. Release* **357**, 249–263 (2023).

53. R. A. Hurle, G. Davies, C. Parr, M. D. Mason, S. A. Jenkins, H. G. Kynaston, W. G. Jiang, Hepatocyte growth factor/scatter factor and prostate cancer: A review. *Histol. Histopathol.* **20**, 1339–1349 (2005).
54. M. Dohi, T. Hasegawa, K. Yamamoto, B. C. Marshall, Hepatocyte growth factor attenuates collagen accumulation in a murine model of pulmonary fibrosis. *Am. J. Respir. Crit. Care Med.* **162**, 2302–2307 (2000).
55. G. dos Santos, M. R. Rogel, M. A. Baker, J. R. Troken, D. Urich, L. Morales-Nebreda, J. A. Sennello, M. A. Kutuzov, A. Sitikov, J. M. Davis, A. P. Lam, P. Cheresh, D. Kamp, D. K. Shumaker, G. R. Budinger, K. M. Ridge, Vimentin regulates activation of the NLRP3 inflammasome. *Nat. Commun.* **6**, 6574 (2015).
56. L.-S. Wang, H. Wang, Q.-L. Zhang, Z.-J. Yang, F.-X. Kong, C.-T. Wu, Hepatocyte growth factor gene therapy for ischemic diseases. *Hum. Gene Ther.* **29**, 413–423 (2018).
57. S. Brown, D. L. Bailey, K. Willowson, C. Baldock, Investigation of the relationship between linear attenuation coefficients and CT Hounsfield units using radionuclides for SPECT. *Appl. Radiat. Isot.* **66**, 1206–1212 (2008).
58. A. C. Best, A. M. Lynch, C. M. Bozic, D. Miller, G. K. Grunwald, D. A. Lynch, Quantitative CT indexes in idiopathic pulmonary fibrosis: Relationship with physiologic impairment. *Radiology* **228**, 407–414 (2003).

**Acknowledgments:** We thank Suzhou Hiscan Information Technology Co. Ltd. for technical support in micro-CT data analysis. **Funding:** This work was supported by the Natural Science Foundation of China (32025021 and T2222021), the National Key R&D Program of China (2023YFC2415700), the China Postdoctoral Science Foundation (2022M723255), and the Ningbo Natural Science Foundation (2023J369). **Author contributions:** Conceptualization: H.B., A.W., and J.L. Methodology: H.B., J.L., and A.W. Investigation: H.B., J.L., and A.W. Visualization: H.B. and J.X. Data curation: H.B., M.W., Z.L., and Y.Z. Formal analysis: H.B. and M.W. Supervision: H.B., A.W., and J.L. Writing—original draft: H.B. Writing—review and editing: A.W., J.L., and H.B. **Competing interests:** H.B., A.W., J.L., J.X., and Z.L. are inventors on a (patent application) related to this work filed by Ningbo Institute of Materials Technology and Engineering, Chinese Academy of Sciences (no. 202410181987.5, Filed 19 February 2024). The other authors declare that they have no competing interests. **Data and materials availability:** All data needed to evaluate the conclusions in the paper are present in the paper and/or the Supplementary Materials.

Submitted 25 April 2024
Accepted 17 July 2024
Published 21 August 2024
10.1126/sciadv.adq0703